

Gamma-ray Analysis of Millisecond Pulsars PSR J0218+4232, PSR B1821-24 and PSR B1937+21

Department of Physics, The University of Hong Kong, Pokfulam
Road, Hong Kong

Wang Wenchao

3030053350

Contents

1	Introduction	1
1.1	Neutron Stars and Pulsars	1
1.2	Emission Mechanism of Pulsars	2
1.2.1	Magnetic Dipole Model	2
1.2.2	Synchrotron Radiation	3
1.2.3	Inverse-Compton radiation	5
1.2.4	A More Sophisticated Model	9
1.3	Millisecond Pulsar	9
1.3.1	P- $\dot{\mathbf{P}}$ Diagram	9
1.3.2	Origin Of Millisecond Pulsars	10
1.3.3	Class II MSPs	11
1.4	Objectives	12
2	Gamma-Ray Analysis	13
2.1	Introduction of The Fermi Gamma-ray Space Telescope	13
2.2	A Brief Introduction of Fermi Data Analysis	15
2.3	Analysis With Fermi LAT	16
2.3.1	Correctness Verification of Data Processing	18
2.3.2	PSR J0218+4232	19

2.3.3	PSR B1821-24	23
2.3.4	PSR B1937+21	27
3	Theory And Simulation	31
3.1	Two-layer Model	31
3.2	Numerical Calculation of Spectra Based on Two-layer Model . .	35
3.3	Pitfalls and Considerations of Doing Numerical Calculation . . .	39
3.3.1	Correctness of Computation	39
3.3.2	Speed of Computation	40
4	Discussion and Future Work	41

Abstract

In the thesis, we mainly introduce our study on the high energy spectra of three millisecond pulsars which are PSR J0218+4232, PSR B1821-24 and PSR B1937+21. The Fermi LAT Pass 8 data was published in 2015 and has lots of advantages over the old Pass 7 data, such as increased effective area and wider energy range. Since the recent gamma-ray spectra analysis of the three MSPs are relatively old (in about 2014), we redo the gamma-ray spectra analysis of the MSPs with 4-year more Fermi LAT observation data and newly published Pass 8 data. As we expected, we obtain better fit results for gamma-ray spectra of the three MSPs with smaller errors and larger test statistic values. Then we briefly introduce a pulsar emission model called two-layer model [5] and do numerical simulation to test the two-layer model using the new observation data. By minimizing the differences between the predictions of the two-layer model and the real data, we fit the independent parameters of the two-layer model, which can help us understand the emission mechanism of pulsars. We find that though the two-layer model is simple, it can generate broad-band spectra of pulsars which are very close to the observation data from Fermi LAT in most energy bands.

Chapter 1

Introduction

1.1 Neutron Stars and Pulsars

Neutron stars are produced by a supernova explosion of massive stars which have about 4 to 8 solar mass. After the supernova explosion, the star leaves a central region. And the central region collapses because of the effect of gravity until protons and electrons combine to form neutrons ($e^- + p \rightarrow n + \nu_e$)—the reason why they are called “neutron stars”. Because neutrons have no electromagnetic force on each other, they can be squeezed very tightly. Therefore, a neutron star has tremendous high density (about $5 \times 10^{17} kg/m^3$) and its diameter and mass is about 20km and 1.4 solar mass respectively. What prevents a neutron star to continue to contract is the degeneracy pressure of neutrons.

Pulsars are fast-spinning neutron stars. Their rotational periods can be from a few milliseconds to several seconds. For example, the rotational period of PSR B1937+21 is about 1.56ms while PSR B1919+21 is approximately 1.34s. As we know, a star can be ripped by centrifugal force if the star rotates too fast. We can estimate lower limit of density of a star with the equation: $\rho = \frac{3\pi}{P^2 G}$, where P is the rotational period of a pulsar. Just for simplicity, we let P be 1s. Then we get $\rho \approx 1.4 \times 10^{11} kg/m^3$. With the knowledge that the density of a white dwarf is about $1 \times 10^9 kg/m^3$ which is smaller than the lower density limit, the observed fast-spinning stars belong to the kind of stars which are much denser than white dwarf. As a result, neutron stars are ideal candidates for pulsars.

More than 2000 pulsars have been found so far. Most of them are in the disk of our Galaxy while we also can find a small portion of them in high latitude, which can be seen clearly in the Fig 1.1. This may because they cannot escape the gravitational potential if their kinetic energy is not large enough. Besides, even though they have large enough velocities to escape from their birth region, there are some probabilities that they become nearly

non-detectable before reaching high latitude.

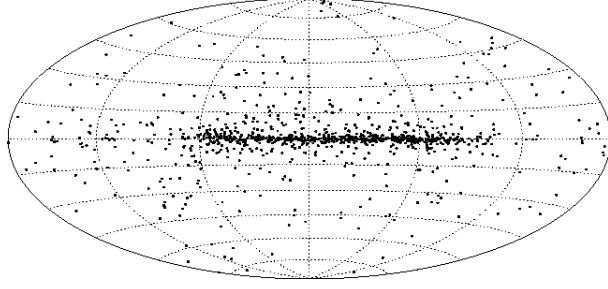


Figure 1.1: *Spatial distribution of some pulsars in galactic coordinate system.*

1.2 Emission Mechanism of Pulsars

Although emission mechanism of pulsars has not been fully understood yet, some models are developed trying to explain observational facts. The following is one toy model that can explain some basic features of pulsars. In this structure, the magnetic dipole model is introduced first, followed by synchrotron radiation and inverse Compton radiation.

1.2.1 Magnetic Dipole Model

Assume a pulsar has a magnetic dipole moment \vec{m} , the angel between rotation axis and direction of \vec{m} is α , its angular velocity is Ω , radius is R and moment of inertia is I . Also by assuming that energy of electromagnetic radiation are all from rotational energy, its spin-down rate can be written as:

$$\dot{\Omega} = -\frac{B_p^2 R^6 \Omega^3 \sin^2 \alpha}{6c^3 I}$$

where B_p is magnetic field strength in the pole of the pulsar. Its surface magnetic field can also be estimated by:

$$B_s = \sqrt{\frac{3c^3 I}{2\pi^2 R^6} P \dot{P}} = 3.2 \times 10^{19} \sqrt{P \dot{P}}$$

where B_s is the strength of surface magnetic field.

In general, a pulsar's spin down rate can be expressed as: $\dot{\Omega} = -K\Omega^n$, where K is a constant and n is called braking index. In magnetic dipole model n is 3 [8]. Then characteristic age of the pulsar can be defined as: $P/2\dot{P}$ in magnetic dipole model. For example, the Crab pulsar's rotation period is about 0.033s and period derivative is $4.22 \times 10^{-13} s/s$. The characteristic age is about 1200 years. The pulsar is remnant of a supernova which is observed by ancient astronomers in 1054 AD, so the record shows that characteristic age can give us order of magnetic estimate of a pulsar's real age.

Although braking index is 3 in magnetic dipole model, most of pulsars' braking index is less than 3 as shown in figure 1.2. The reason is that if a pulsar's spin down is completely because of pulsar wind, the braking index is 1. Thus, the real braking index should be a combination of 1 and 3, which is usually less than 3 [4].

Pulsar	n_{obs}	Ω s^{-1}	$\dot{\Omega}$ 10^{-10}s^{-2}
PSR B0531+21 (Crab)	2.51 ± 0.01	30.22543701	-3.862283
PSR B0540-69	2.14 ± 0.01	19.8344965	-1.88383
PSR B0833-45 (Vela)	1.4 ± 0.2	11.2	-0.157
PSR B1509-58	2.839 ± 0.001	6.633598804	-0.675801754
PSR J1846-0258	2.16 ± 0.13	3.0621185502	-0.6664350
PSR J1833-1034	1.857 ± 0.001	16.159357	-0.5275017
PSR J1119-6127	2.684 ± 0.001	2.4512027814	0.2415507
PSR J1734-3333	0.9 ± 0.2	0.855182765	-0.0166702

Figure 1.2: *Braking index of some pulsars.*

1.2.2 Synchrotron Radiation

Synchrotron radiation is a special case of cyclotron radiation when particles' speed is comparable to the speed of light. Because of the relativistic beaming effect, we will observe a very short radiation pulse when speed of particles is large. We only aim to analyze the spectrum properties of MSPs, so we focus on the spectrum property of synchrotron radiation. The power spectrum of a single electron can be described by the function 1.1

$$P(\nu) = \frac{\sqrt{3}e^3 B \sin \alpha}{mc^2} \left(\frac{\nu}{\nu_c} \right) \int_{\nu/\nu_c}^{\infty} K_{5/3}(\eta) d\eta \quad (1.1)$$

where ν_c is the critical frequency and $K_{5/3}$ is modified Bessel function. The critical frequency can be expressed by the function 1.2

$$\nu_c = \frac{3}{2} \gamma^2 \nu_{cyc} \sin \alpha \quad (1.2)$$

where α is the pitch angle and the ν_{cyc} is the frequency of corresponding cyclotron radiation.

These function does not give us very much information because of the integration of the modified Bessel function. We let $x = \nu/\nu_c$ and fix the environment variables such as magnetic field (B), the function 1.1 becomes:

$$P(\nu) = C \times x \int_x^{\infty} K_{5/3}(\eta) d\eta \quad (1.3)$$

where C is a constant dependent on B . Thus, in order to analyze the power spectrum of synchrotron radiation, we only concentrate on the later part, which is

$$F(x) = x \int_x^\infty K_{5/3}(\eta) d\eta \quad (1.4)$$

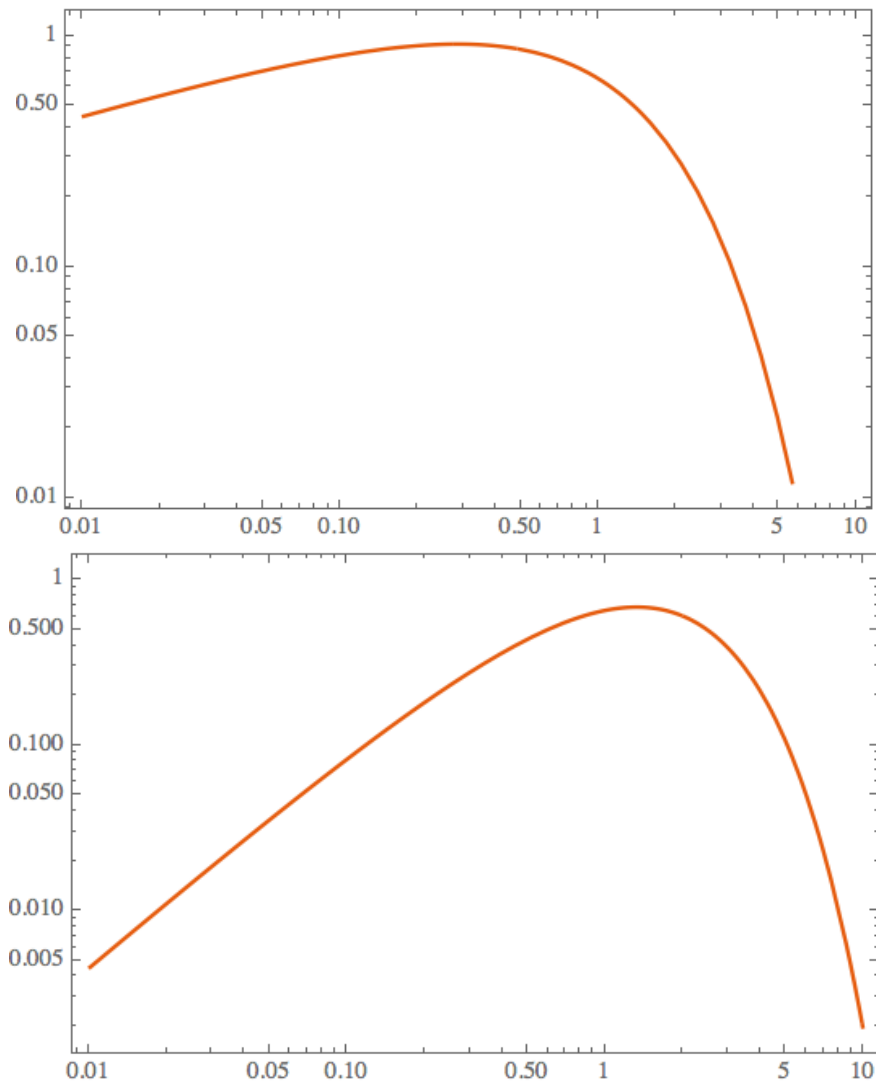


Figure 1.3: According to the function 1.4, top: $F(x)$; bottom: $xF(x)$.

< change > should change the style of the Fig.. < /change >

The top figure 1.4 describes the general shape of power spectrum of synchrotron radiation. When the frequency is larger than the critical frequency ν_c , the power goes down dramatically. However, the top figure does not show the information that at what frequency the electron emit the strongest power, which is in the bottom figure. The bottom figure shows that the energy most energy emitted around critical frequency.

In reality, synchrotron radiations are not generated by a single particle. We describe the number density distribution of electrons with respect to energy

by a single power-law model as the function 1.5 shown.

$$N(E) \approx CE^{-\delta} \quad (1.5)$$

For simplicity, we set the ambient magnetic field B to be a constant and make an approximation that all radiations are at a single frequency:

$$\nu \approx \gamma^2 \nu_{cyc} \quad (1.6)$$

where the meaning of ν_{cyc} is the same as function 1.2. Our objective is to know the relationship between total power of all electrons and their radiation frequency. We describe the relationship as the function 1.7

$$-P(E) N(E) dE = Q_\nu d\nu \quad (1.7)$$

$$P(E) = \frac{4}{3} \sigma_T \beta^2 \gamma^2 c U_B \quad (1.8)$$

where σ_T is electron Thompson scattering section, U_B is energy density of the environment magnetic field, Q_ν is the emission coefficient of synchrotron radiation and $E = \gamma m_e c^2$. With function 1.6, we have

$$P = \frac{dE}{d\nu} = \frac{m_e c^2}{2\sqrt{\nu\nu_{cyc}}} \quad (1.9)$$

Combine the function 1.9 and 1.7 we get:

$$Q_\nu = \frac{4}{3} \sigma_T \beta^2 \gamma^2 c U_B \frac{m_e c^2}{2\sqrt{\nu\nu_{cyc}}} N(E) \quad (1.10)$$

By ignoring constants in the function 1.7 we have

$$Q_\nu \propto \nu^{(1-\delta)/2} \quad (1.11)$$

The function 1.11 shows that if the number density electrons is a power-law distribution, the spectrum of synchrotron radiation is also a power-law model.

1.2.3 Inverse-Compton radiation

If a energetic relativistic photon collides with a charged particle from an proper incident angle, the photon's energy decreases and direction changes. This is a process of Compton Scattering. Inverse-Compton radiation is the opposite process by which a low energy photon gained energy from an ultra-relativistic electron.

As the Fig. 1.4 showing, in the laboratory frame (S), the incident angle and energy of a photon is θ and $h\nu$ respectively. The speed of the electron is

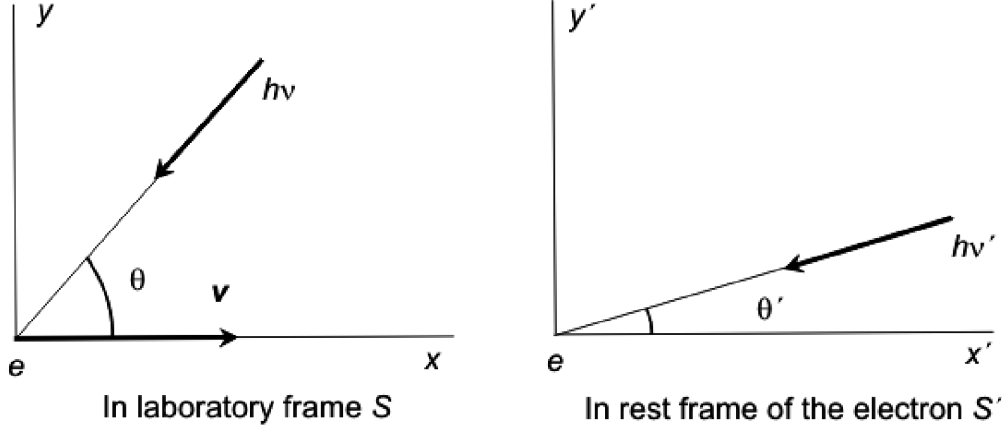


Figure 1.4: *Inverse Compton Diagram* <Notice>this figure is from internet</Notice>

v . In the electron rest frame (S'), we change the denotation to θ' , $h\nu'$ and. Also, let the position of the electron be the origin point of S' . We can study the whole process in the S' frame, the transfer the result to the S frame by Lorentz transformation.

In the S' frame, the electron is at rest so its energy is $m_e c^2$. For Inverse Compton scattering, the energy of an incident photon (less than several keV) is much less than the rest energy of an electron (about $0.51MeV$) and the relationship can be expressed by $h\nu' \ll m_e c^2$. Therefore, this can be treated as Thompson Scattering process. Let the Poynting vector of incident photons be \vec{S}' and their energy density be U'_{rad} , we have equation 1.12

$$\vec{S}' = cU'_{rad} \quad (1.12)$$

The electron absorbs the energy of the incident photons and then be accelerated. Thus the accelerated electron will emit part of energy taken from incoming photons and the power of scattered radiation is denoted as P' . The ratio can be described by Thompson Scattering cross section σ_T which is:

$$\sigma_T = \frac{8\pi}{3} \left(\frac{e^2}{m_e c^2} \right)^2 \quad (1.13)$$

and the relationship between the electron radiation power and incoming photon energy flux can be described by the equation 1.14

$$P' = |\vec{S}'| \sigma_T \quad (1.14)$$

Combine the equation 1.12 and 1.14, the radiation power emitted by the electron is:

$$P' = c\sigma_T U'_{rad} \quad (1.15)$$

Then we need to find the relationship between frame S and S' . It mainly contains 2 parts: the relationship between P , P' and U_{rad} , U'_{rad} . Since $P =$

dE/dt and dE/dt is Lorentz invariant in inertial frame, we know:

$$P = P' \quad (1.16)$$

Now we hope to write U'_{rad} in terms of U_{rad} . U_{rad} is comprised by energy of a single photon and photon density. In the flowing analysis, all the denotations are correspondent to 1.4 According to the relativistic Doppler shift formula, we have:

$$h\nu' = (h\nu) \gamma (1 + \beta \cos \theta) \quad (1.17)$$

where $\beta = v/c$ and γ is Lorentz factor of an ultra-relativistic electron. Then we calculate the photon density. In the frame S' , the photon density is inverse proportional to the time interval (Δt) between 2 photon strike the electron since total number of photons is Lorentz invariant. In laboratory frame S , we consider 2 photons collide with the electron at the 4-dimension vector of $(x_1, 0, 0, t_1)$ and $(x_2, 0, 0, t_2)$. According to the Lorentz transformation between inertial frames:

$$\begin{cases} x = \gamma (x' + \beta ct') \\ y = y' \\ z = z' \\ t = \gamma \left(t' + \frac{\beta x'}{c} \right) \end{cases} \quad (1.18)$$

And since we set $x' = 0$, from equation 1.18, the 2 events of 2 successive photons collide with the electron can be expressed as: $(\gamma vt'_1, 0, 0, \gamma t'_1)$ and $(\gamma vt'_2, 0, 0, \gamma t'_2)$. As the Fig 1.5 showing, the time interval of two successive photons (reciprocal of frequency) in frame S is:

$$\begin{aligned} \Delta t &= (t_2 - t_1) + \frac{(x_2 - x_1) \cos \theta}{c} \\ &= \gamma (t'_2 - t'_1) + \frac{\gamma v (t'_2 - t'_1) \cos \theta}{c} \\ &= \Delta t' \gamma (1 + \beta \cos \theta) \end{aligned} \quad (1.19)$$

The equation 1.19 shows that the relationship of photon number density between frame S and S' is:

$$n' = n \gamma (1 + \beta \cos \theta) \quad (1.20)$$

Combine the equation 1.20 and 1.17 we can transfer the incident photon energy density from frame S to S' according to the equation 1.21

$$U'_{rad} = U_{rad} [\gamma (1 + \beta \cos \theta)]^2 \quad (1.21)$$

In the equation 1.21, the incoming photon energy density is a function of incident angle (θ), in order to get the total photon energy density, we integrate the equation over θ . Then we get:

$$U'_{rad} = \frac{4}{3} U_{rad} \left(\gamma^2 - \frac{1}{4} \right) \quad (1.22)$$

By combining the equation 1.22 and 1.15 we know the total scattered radiation power is:

$$\begin{aligned} P' &= P \\ &= \frac{4}{3}\sigma_T c U_{rad} \left(\gamma^2 - \frac{1}{4} \right) \end{aligned} \quad (1.23)$$

As mentioned before, P' and P are total radiation power after scattering. Before the low energy gain photons, they give away some energy first which is $\sigma_T c U_{rad}$. Therefore, we have to subtract this value from the equation 1.23 to calculate the rate of net energy gain, which is described by the equation 1.24.

$$\begin{aligned} P' = P = \frac{dE}{dt} &= \frac{4}{3}\sigma_T c U_{rad} \left(\gamma^2 - \frac{1}{4} \right) - \sigma_T c U_{rad} \\ &= \frac{4}{3}\sigma_T c U_{rad} \beta^2 \gamma^2 \end{aligned} \quad (1.24)$$

If we compare the equation 1.24 with 1.9, we find that the form is very similar between these two equations.

$$\frac{P_{IC}}{P_{sync}} = \frac{U_{rad}}{U_B} \quad (1.25)$$

where U_B is the energy density of environment magnetic field.

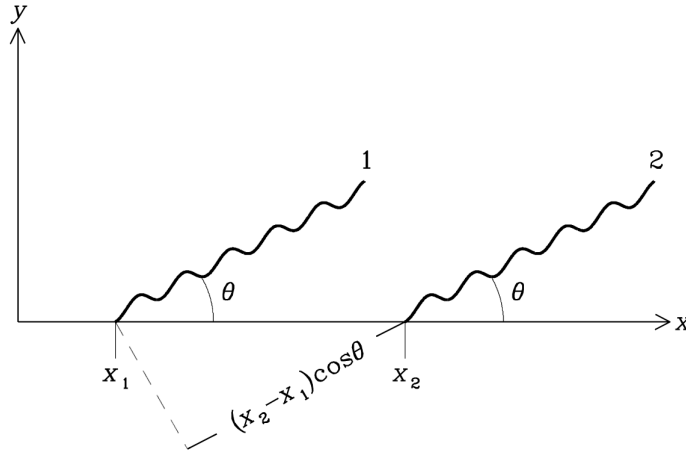


Figure 1.5: Two photons collide with an electron. In the frame S' , two photons collide with a rest electron successively. In the frame S , the electron is no longer at rest and the positions of the two events are x_1 and x_2 <Notice>the Fig. is from internet</Notice>

<add>spectrum property, shape</add>

1.2.4 A More Sophisticated Model

It is oversimplified to regard a pulsar as a magnetized sphere rotating in vacuum. Actually, there are plenty of charged particles in a pulsar's magnetosphere which co-rotate with the pulsar. The creation of charged particles can be described by the following steps [7].

1. The co-rotating charged primary particles emit gamma-ray by curvature radiation because of acceleration in super strong magnetic field.
2. In super intense magnetic field, the high energy photons decay into electrons and positrons which are called secondary particles by the process: $\gamma + (B) \rightarrow e^+ + e^- + (B)$. Synchrotron photons can be emitted by these secondary particles.
3. Secondary particles are also accelerated in strong magnetic field which is just like primary particles. As a result, these charged particles can create more secondary particles.

This chain of process is quite efficient to produce charged particles and pulsar's magnetosphere is filled with plasma as a consequence. So, it is natural to think of the distribution of charges in pulsar's magnetosphere. A characteristic charge density $\rho_{GJ} = -\frac{\vec{\Omega} \cdot \vec{B}}{2\pi c}$ is called Goldreich-Julian density. This charges can offset part of electric field (E_{\parallel}) which is parallel to magnetic field. There is some region in the magnetosphere called "outer gap" where ρ_{GJ} is so small that it can't screen E_{\parallel} effectively. As a result, the secondary particles can be accelerated at a very large velocity (Lorentz factor $\gamma \sim 10^7$) and emit gamma-ray. Photons in outer gap can also create electrons and positrons by the process: $\gamma + \gamma \rightarrow e^- + e^+$. At the outer gap, one-photon pair production can't happen because magnetic field is too weak in this region.

1.3 Millisecond Pulsar

1.3.1 P- \dot{P} Diagram

P- \dot{P} diagram is an important tool for analyzing evolution of pulsars. Period (P) and time derivative of period (\dot{P}) are two of pulsars' important characteristics. Analyzing the position of a pulsar in P- \dot{P} diagram can give some valuable information such as which evolution stage the pulsar is in or the type of the pulsar, etc. The Fig. 1.6 is an example of P- \dot{P} diagram. The horizontal axis is pulsars' rotation periods and the vertical axis is time derivative of rotation periods. In this P- \dot{P} diagram, the negative slope lines represent the strength of surface magnetic field while the positive slope lines represent the characteristic age of pulsars. The following is a short explanation for this. From previous discussion, we have known that the characteristic age of a pulsar is $\tau = -P/\dot{P} = P/(-\dot{P})$, so line of constant τ is a set of straight lines with

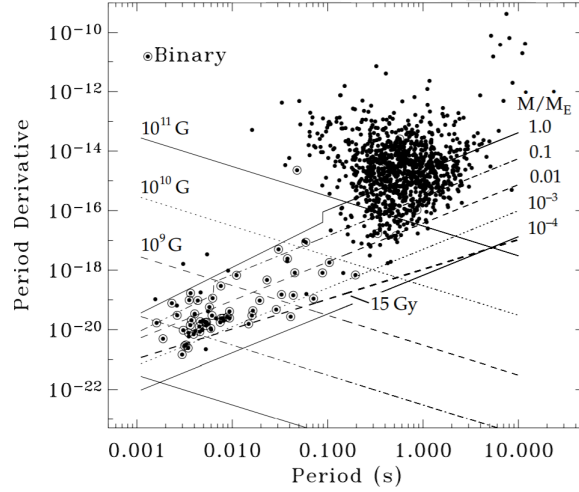


Figure 1.6: *Position of pulsars in P - \dot{P} diagram*

equal positive slope. We also know $B \propto \sqrt{P\dot{P}}$, therefore the line of constant B should be a part of hyperbola. When \dot{P} is very small, the hyperbola looks like a straight line with negative slope.

This figure shows that most pulsars lie in the position about $1s, 10^{-14}s/s$. At the same time, a couple of stars lie at the bottom-left of the Fig.—these are millisecond pulsars (MSP). Their rotation periods are about 1-20 milliseconds. It is believed that MSPs are spun up by accretion of mass from its companion star. In the above P - \dot{P} diagram, we can observe that millisecond pulsars' surface magnetic field are about 3 to 4 orders of magnitude lower than those of normal pulsars. However, an MSP has a relative strong magnetic field near its light cylinder. The reason is that an MSP's radius of light cylinder ($R_{lc} = c/\omega$) is much smaller than a normal pulsar's because of its short rotation period and the magnetic field near light cylinder can be estimated as $B_{lc} \sim (R/R_{lc})^3$. At the same time, pulsars' emission mechanism is closely related to their magnetic field near light cylinder. As a result, like a normal pulsar, an MSP also have broadband spectrum from radio to gamma rays.

1.3.2 Origin Of Millisecond Pulsars

From pulsars' emission mechanism, we know that magnetic field of a pulsar decreases with time while the spin period increase with time. But MSPs' spin period is much shorter than normal pulsars and surface magnetic field is a lot weaker. This makes an MSP seem to be both young and old. As a result, people think millisecond pulsars are old pulsars spun up by its companion. The companion star transfer mass and angular momentum to accelerate the pulsar. Therefore, the aged pulsar can spin faster gradually.

Mass Transfer And Accretion In Binary Systems

X-ray binaries are a type of binary systems that is luminous in X-ray band. There are several kinds of X-ray binaries including low mass X-ray binaries (LMXB) and high mass X-ray binaries (HMXB). The way of transferring mass is different in these two types of systems. Before discussing mass transfer, we need to know a little bit about Roche Lobe. The Fig. 1.7 is a schematic diagram of Roche lobe.

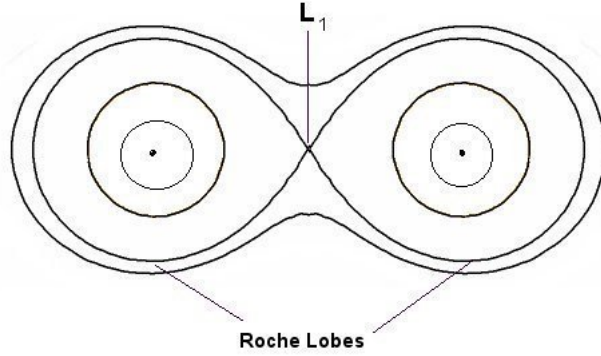


Figure 1.7: Schematic diagram of Roche lobe. L_1 is called inner Lagrange point which is the intersection of equipotential lines of star A and B.

We call two stars in an LMXB as A and B respectively for convenience. It is obvious that if an object is close to star A, the gravitational influence of A is so strong that we can nearly ignore the effect of star B. Similarly, this is true for star B. As a result, there must be a point where the effect of star A is equal to star B which is called inner Lagrange point [6]. The two volumes inside the largest equipotential lines of A and B are called Roche lobe. If star B cross its Roche lobe, then its mass will be attracted by A thus mass transfer between A and B happens. We should notice that this is the main way of mass transfer in LMXB. While in HMXB, the mass can be transferred by strong wind of the massive companion star.

What should be noted is that mass transfer can change the distance between two companion stars. If low-mass star transfer mass to high-mass companion star, the orbital separation will be large. This can actually stop mass transfer and is like negative feedback. On the contrary, mass transfer from high-mass star to low-mass star will shrink the orbital distance.

1.3.3 Class II MSPs

Radio emission are usually considered to be emitted above the polar cap, which means radio emission and gamma-ray emission are from different location of pulsar's magnetosphere. However, there are about 10 sources showing aligned

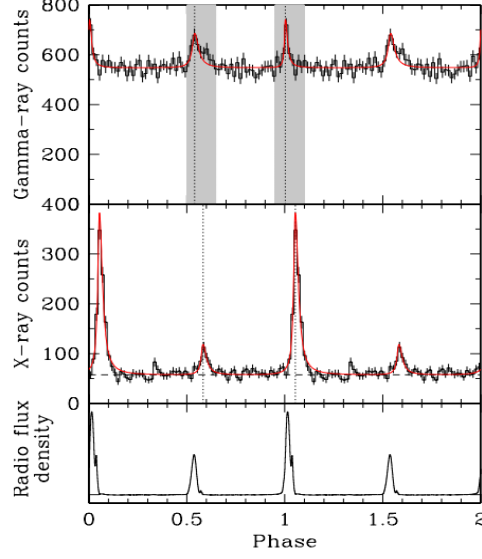


Figure 1.8: *Pulse profiles of PSR B1937+21 in radio, X-ray and gamma-ray.*

pulse profiles in radio and gamma-ray implying that radio emission may produced from outer magnetosphere and they are called Class II MSPs [3]. These pulsars have strong magnetic field near the light cylinder. The Fig. 1.8 is an example of aligned pulse profile.

1.4 Objectives

The three millisecond pulsars J0218+4232, B1821-24 and B1937+21 show broadband spectra in all radio, X-ray and gamma-ray bands. Fermi LAT gives us additional data and tools to do gamma-ray analysis for the pulsars. Lots of research have been done on the three MSPs, however, many of them are a little bit 'old'. In year 2015, Fermi team released Pass 8 data including many improvements. According to the *Fermi official website*, Pass 8 dataset includes improved event construction, better energy measurement and significantly improved effective area. Additionally, we have more observation Fermi LAT data. As a result, it is reasonable to redo the gamma-ray analysis with newer dataset and more observation data and gain more reliable results.

Therefore, my main objective is to use the new tools and data to redo the gamma-ray analysis of the three MSPs listed above. Then, I will do a numerical simulation based on a theoretical model called two-layer model and test if the new observation data is consistent with the model. And finally, with the help of the two-layer model and numerical simulations, I will generate broadband spectra (including hard X-ray band and gamma-ray band) for all the three MSPs.

Chapter 2

Gamma-Ray Analysis

As mentioned before, because of the very short rotation periods, MSPs have very small light cylinder radii compared with normal pulsars. As a result, their emission mechanisms are similar to normal pulsars, especially for my target objects — PSR J0218+4232, PSR B1937+21 and PSRJ1824-2452 which are among the fastest spinning MSPs. Therefore, as normal pulsars, these three pulsars are bright in Gamma-Ray band so it is convenient for us to analyze the spectra properties of them in gamma-rays.

2.1 Introduction of The Fermi Gamma-ray Space Telescope

The Fermi Gamma-ray Space Telescope was launched on June 11, 2008 and opened a new window of studying supermassive black-hole systems, pulsars and so on. Its original name was Gamma-ray Large Area Space Telescope (GLAST) and changed to Fermi Gamma-ray Space Telescope in honor of a great scientist Enrico Fermi.

The Fermi Gamma-ray Space Telescope contains two parts: Gamma-ray Burst Monitor (GBM) and Large Area Telescope (LAT), which is the primary components and is at least 30 times more sensitive than all gamma-ray telescopes launched before. We only use LAT for our purposes. So we focus on the LAT instrument, which contains four main subcomponents including tracker, calorimeter, anti-coincidence detector and data acquisition system. The reason why the telescope is designed in this way is that high-energy gamma-rays cannot be refracted by lens or mirrors. As a result, the way that the Fermi LAT operates is totally different.

The following figure 2.1 demonstrates the very basic idea of the Fermi LAT working principles.

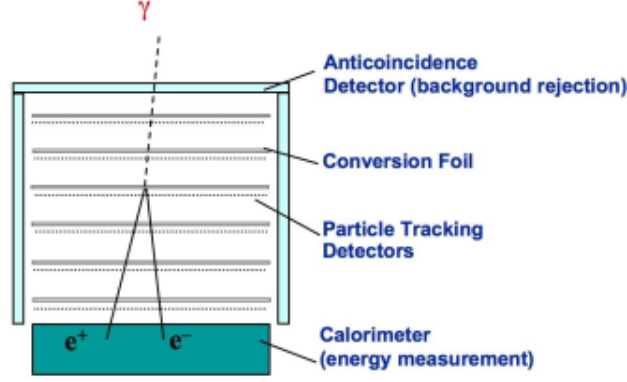


Figure 2.1: *Light curve of module A*

- Gamma-ray photons can enter the anti-coincidence detector freely while cosmic-rays will generate signals which can tell the data acquisition system to reject these particles. In this way, the Fermi LAT can distinguish the gamma-ray photons and high energy cosmic rays and the confidence is over 99.9%.
- The conversion foil (shown in the Fig. 2.1) can convert the gamma-ray photons into electron and positron pairs. This procedure makes it possible to determine the directions of the coming gamma-ray photons.
- The tracker (particle tracking detectors in the Fig. 2.1) records the positions of the electrons and positrons generated from the gamma-ray photons. There are many trackers so the paths of a particle can be constructed.
- The electrons and positrons reach the calorimeter hence their energies are also measured. Therefore, the energies of the original gamma-ray photons can also be calculated.
- The data acquisition system rejects unwanted particles such as cosmic rays by the method we mentioned before. Also, photons come from the Earth's astronomers are also rejected.

For a telescope, the ability of measuring the light direction and energy is very crucial. From the above descriptions of the Fermi LAT working principles, we know that the preciseness of construction of particles' path heavily influences how good we can measure the direction of photons. And this process is greatly dependent on algorithms, which means that with the improvements of software, the sensitivity of the telescope can also be improved. The Pass 8 data was released on June 24, 2015. It is an reprocessing of the entire Fermi

mission dataset with better energy measurements, larger effective area, wider energy range and so on. This is part of the reason why I will redo the analysis of the three MSPs.

2.2 A Brief Introduction of Fermi Data Analysis

We not only want to analyze observation data from Fermi LAT but also study spectra models of our interested sources. We do spectra analysis by comparing our model with the observation data based on maximum likelihood principal.

When doing Fermi data analysis, we basically dealing with 2 "threads". The first is processing observation data and the second is generating photon distribution based on our models. Cleaning data is straightforward including select data, filter data with good time intervals(GTI), generating count maps and so on. Generating model-based count maps and count cubes needs a little bit more effort and mainly includes the following procedures.

Firstly, we need to generate a spectra model of all sources in our region of interest (ROI). The model basically describes how strong each source is in different energy bands and different positions. However, the model alone is not very helpful and we have to know other informations in order to get simulated photon distribution.

Since we are going to compare our simulation with the observation data, we have to take the telescope influence into account. For example, effective area of telescope decreases when we are away from the optical axis. In addition, inclination angles and observation time have a direct effect on the number of photon counts. In short, after we get the simulated photon distribution from our model, we have to transfer the simulation into the "real simulation" by applying the telescope functions.

After we get the photon distribution simulation, we can then do comparisons in order to get the maximum likelihood. We divide the total energy band into many smaller bins and denote the number of photon counts in observation data as n_i , so that $\sum_i n_i = N$, where N is the total number of photons we observed. The observed number of photon counts in i th bin is a Poisson distribution with a mean of m_i . Actually, the value m_i is the expected number of photon counts from our spectra model. Therefore, the distribution for i th bin can be expressed by the function 2.1, where $P_i(n_i)$ is the possibility of observing the n_i photon counts for the i th bin.

$$P_i(n_i) = \frac{e^{-m_i} m_i^{n_i}}{n_i!} \quad (2.1)$$

As a result, it is not hard to generalize the possibility for each bin to all

bins, just by multiplying the possibilities for different bins.

$$\begin{aligned}
P_{total} &= \prod_i P_i(n_i) \\
&= e^{\sum_i m_i} \prod_i \frac{m_i^{n_i}}{n_i!}
\end{aligned} \tag{2.2}$$

In the function 2.2, n_i s are directly from observation data so they usually can not be changed during the binned likelihood analysis. However, by changing our model, the m_i s can be altered. Hence, our aim is to tweak the spectra model in order to make the total possibility P_{total} as large as possible.

This is the basic idea and procedure of doing Fermi data analysis. After doing these, we can go further such as testing how significant our target is by creating TS maps. The thesis basically follows the procedures.

Before finishing this part, let's take a look at what a TS map is. TS stands for "Test Statistic" which can be expressed as the function 2.3

$$TS = -2 \ln \frac{L_{max,0}}{L_{max,1}} \tag{2.3}$$

where $L_{max,0}$ and $L_{max,1}$ is the maximum likelihood of models in which our target source is not included and included respectively. According to the function 2.3, the larger the TS value is, the larger $L_{max,1}$ is, which means that the probability of existence of the target source is larger. In order to generate a TS map, we divide the whole map into many sub-grids. In each sub-grid, the algorithm basically does 2 things. The first procedure is calculating the maximum likelihood directly based on our spectra model ($L_{max,0}$). Then it adds an imaginary source, fit the source and get the maximum likelihood ($L_{max,1}$). In the end, it can get the TS value for the sub-grid using the function 2.3.

After having the TS values for each sub-grids, we can generate a TS map just by rendering colors according to the each grid's TS value. By comparing TS values of each grid in a TS map, we can determine where our target source is most likely to be and how large the probability is.

2.3 Analysis With Fermi LAT

In this section, my main objective is to show the results of my analysis. Before doing so, it is appropriate to briefly introduce some terminologies.

- The first is count maps. A count map is basically generated by the following steps. Firstly we choose a pixel with a certain size. Then we check each photon's direction to determine if the photon is in this pixel.

If it is in the pixel, the photon counts of the pixel will add one. So more photons fall within the pixel, the more photon counts the pixel has, hence the brighter the pixel is. By doing the same thing for every pixel, a count map is generated. A count map let us know what we have observed intuitively and gives us a very basic idea of if we get the wanted data.

- A count cube is very similar to a count map, except that a count cube is divided in many energy bands. For example, a dataset whose energy is from 100MeV to 100GeV can be divided into 30 bins. We can generate a count map in each energy bin, so we have 30 count maps. In other words, we can regard a count cube as multiple count maps. A count cube's advantage over a count map is that we can observe distribution of gamma-ray photons in different energy range.
- TS value provides us a way to test if our target source is observed. The definition of TS value is: $TS = -2 \frac{\ln L_{max,0}}{\ln L_{max,1}}$, where $\ln L_{max,0}$ is the maximum likelihood value without the target source while $\ln L_{max,1}$ is the maximum likelihood value with the target source. According to the equation, the smaller the ratio of $\ln L_{max,0}$ and $\ln L_{max,1}$, the larger the TS value is. Therefore, a larger TS value statistically means that our aimed source is observed.
- `< mayAdd >` may have more items `< /mayAdd >`

The basic idea of fitting spectra parameters is to make the count cube generated by the model be as similar to the observation data as possible. The calculation process can be summarized as follows. First of all, we have to generate a spectral model for every source in the region of interest based on the Fermi database. The database includes LAT four-year Point Source Catalog (3FGL), Galactic diffuse emission (gll_iem_v06.fits) and isotropic emission (iso.P8R2_SOURCE_V6_v06.txt). Then we can produce a count cube based on the model. Generally speaking, the difference of the count cubes between the model and observation is obvious. Then, the Fermi software adjusts the parameters to make the difference smaller. Until the errors are acceptable, the software outputs the final fitted parameters.

We use a power-law-exponential-cutoff (PLExpCutoff) model to fit the observation data and it is a special case of power-law-super-exponential-cutoff (PLSuperExpCutoff) model. The spectrum of PLSuperExpCutoff can be described by the function:

$$\frac{dN}{dE} = N_0 \left(\frac{E}{E_0} \right)^{\gamma_1} \exp \left(- \left(\frac{E}{E_c} \right)^{\gamma_2} \right) \quad (2.4)$$

where N_0 is prefactor, E_c is the cutoff energy and the E_0 is a scale parameter. PLExpCutoff model is the special case where $\gamma_2 = 1$. Our aim is to fit the parameters N_0 , E_c and γ_1 to make the model be more consistent with observation data.

2.3.1 Correctness Verification of Data Processing

Before analyzing the observation of my target sources, it is reasonable to test if my procedure of data processing is right or not. In order to do so, I try to do analysis for 2 pulsars whose names are J0007+7303 and J0534+2200. The reason I choose these two pulsars is that in previous study, they are bright and easy to detect with a large TS value — the TS values are 43388 and 102653 for J0007+7303 and J0534+2200 respectively. The data is from *this paper* .

In the spectra fit process, I do not use the same fit parameters as the the paper, (for instance, the number of free parameters are different) however, I get the similar result as the table 2.1 showing. In this table, I use the observation data from 2009-01-01 to 2013-02-01 in order to try to be consistent with the paper. In addition, I also fit spectra with data end up to 2018-02-01 to test how much improvement the Fermi Pass 8 Lat data has over the previous version. The results of year 2018 data is showed in table 2.2.

	Test			Paper		
	Γ	E_c (MeV)	TS	Γ	E_c (MeV)	TS
J0007+7303	1.30 ± 0.02	2010 ± 85	96979	1.4 ± 0.1	4700 ± 200	43388
J0534+2200	2.07 ± 0.01	9880 ± 572	239015	1.9 ± 0.1	4200 ± 200	102653

Table 2.1: *The Spectra Fit Result. In the thesis, in order to make data analysis be more convinient, I use some pipeline scripts to deal with the observation data. The "Test" column shows the results generated by using the pipeline scripts. The "Paper" column lists the corresponding spectra properties from the paper [1]. According to the standard PLSuperExpCutoff model (described in equation 2.4, Γ is photon index and E_c is cutoff energy.*

	Γ	E_c (MeV)	TS
J0007+7303	1.34 ± 0.02	2204 ± 67	210166
J0534+2200	2.01 ± 0.01	9173 ± 372	449946

Table 2.2: *Fit Results With Data From Year 2009 To Year 2018. The physical meanings of Γ and E_c are the same as the table 2.1.*

The table 2.1 and table 2.2 mainly show 2 pieces of information. Firstly, my procedure of dealing with observation data has no big problems, so basically I can trust fit results of my target sources. Secondly, the Fermi Pass 8 Lat Data has improves the accuracy a lot. For example, as the table 2.1 showing, the photon indexes are 1.30 ± 0.02 and 1.4 ± 0.1 , which means that the errors reduce a lot. Additionally, the TS value is more than double as before.

2.3.2 PSR J0218+4232

Our ROI is a circle with radius of 20° and all parameters of sources which are 8° outside of the center are fixed. For sources within 8° , their parameters are the same as the default values. In our case, there are 7 point sources which have free parameters. In the Fig. 2.2, the green circles represent those free sources. We need to notice that in the outer parts of the count map, there are some of very bright sources which have no free parameters. The reasons is that the they are so far away from our target source that the Fermi telescope can distinguish if a photon comes from the target source or the outer sources. As a result, we do not need to fit any parameters for those outer sources. However, it is another case for the nearby sources.

Count Maps And Count Cubes

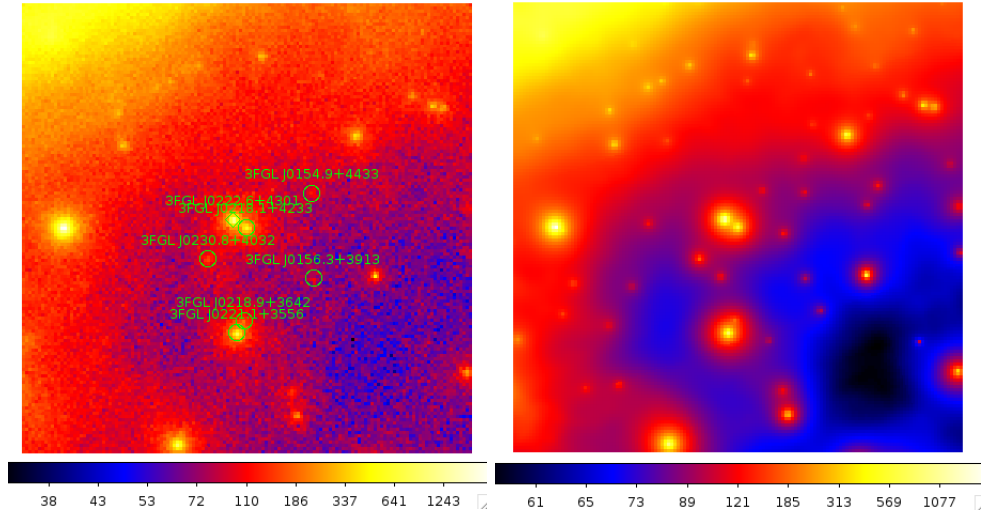


Figure 2.2: The count map of PSR J0218+4232 (left) and the count map generated by the model. In the left figure, the green circles represent free sources. The Fig. in the right is count map generated according to our fitted spectra model. The size of the Fig. is $141 \text{ pixels} \times 141 \text{ pixels}$, and each pixel is $0.2^\circ \times 0.2^\circ$.

In the left of the Fig. 2.2 is the count map of PSR J0218+4232. In the center of the left figure, we can clearly see our target source. The dimension

of the Fig.s seems to be weird and the reason why we have 141 pixels for both x and y axis is that we select a circle region from the original data. However, when we generate a count map, we have to assign the sizes for x and y axis separately, which means that our a count map is actually rectangular. As a result, we have to crop a rectangular from the original circle region and in this case, we choose the rectangular as a square.

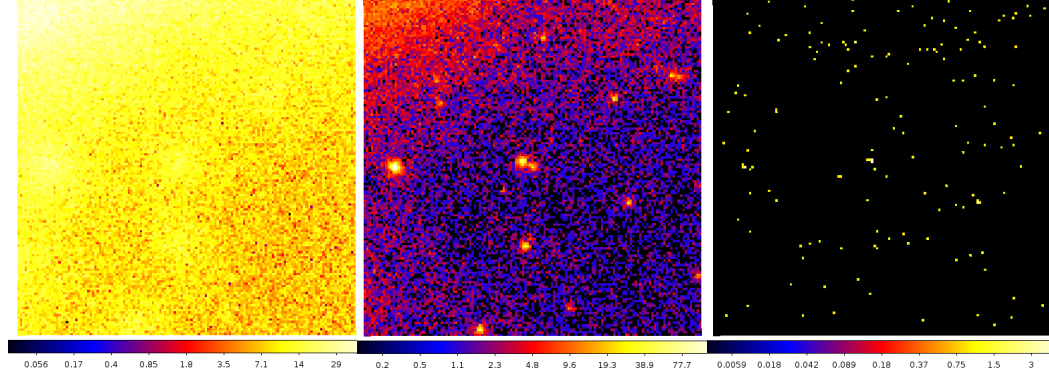


Figure 2.3: Three figures of PSR J0218+4232's count cube. The energy range of the Fig. in the left: 100~123MeV, middle: 1.873~2.310GeV, right: 35.11~43.29GeV.

The Fig. 2.3 is a comparison between PSR J0218+4232's count maps in different energy bands. The count map in about 100MeV is so messy that we can hardly distinguish our target source while above 30GeV there are so few photons that there is not a clear sign of the source. We choose three circle regions whose centers are the our target sources and the radii are 1000 " for all of the three figures and then calculate the total photon counts of the selected regions. As the following table 2.3 shown, though total number of photon counts around our target source is similar between the left and middle maps, the number of counts per energy is much different. Since there are few photons in high energy band (above 50 GeV) compare to other energy bands, we focus more on the lower energy part.

	Left	Middle	Right
Total counts	78	93	0
Energy range (MeV)	100~123	1873~2310	35110~43290
Counts / MeV (MeV^{-1})	3.39	0.213	0.000

Table 2.3: Photon counts of count maps in different energy bands.

Spectra Fitting

The Fig. 2.2 shows that the fit result of the model is similar to the observation. However, there are lots of small red pixels in the left figure (generated directly by the observation data) while the right figure is very "clean". This means that a lot of photons are thought as generated by the modeled source. Thus in our model, the sources are generally slightly brighter than the observation. However, our target source is an exception. In the region we have used before (the center is the target source, and the radius is $1000''$), the total photon count in the left figure is 1815 compare to 1737 in the right figure.

The reason why the count map generated directly by the observation data is a lot more messy is that our source model is generated according to the Fermi database and their spatial position is fixed. This means that if a photon comes from a particular direction and there is no any known pulsar in that direction, this photon has to be classified to other directions and there is a modeled source in the direction. Thus, the spatial positions of photons are different between the observation and the model and the count maps generated directly from models are usually cleaner.

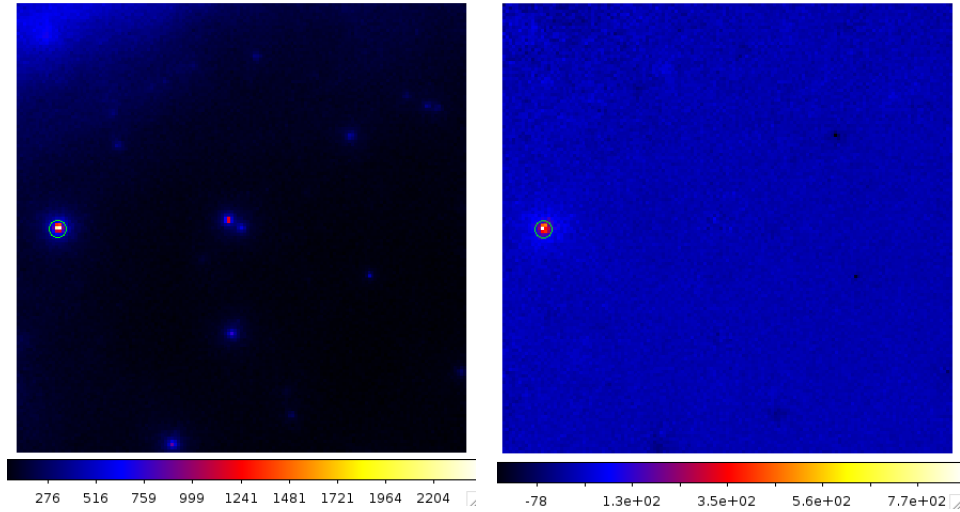


Figure 2.4: *The count map and residual map of PSR J0218+4232. The Figs are in linear scale in order to compare the residual map between the original count map more intuitively. The left figure is the count map and the right figure is the residual map and it shows the difference between the observation and the model. It is created by directly subtracting the photon counts of each pixel between the count maps of observation data and the model. The green circle regions represents (the regions are completely the same in the two figures) the largest region in the residual map and its radius is $2000''$.*

The Fig. 2.4 generally describes how well our model is compared to the observation data. There are some black dots and bright dots in the residual map showing the differences between our spectral model and the data. In

the residual map of figure 2.4, most differences of absolute photon counts are small, however, in the green circle region, the absolute value is large — 6003. This means that in this region, the number of photon counts in the observation data (21525) is 6003 larger than in our model. And the This is not negligible since it is nearly 28% of the original photon counts. Does this mean that our model is not good? The answer should be yes, however, this does not mean our fit is not good since the model parameters in this region is fixed and the fixed values are from the Fermi LAT 4-year Point Source Catalog. Hence, the difference shows some problems of our spectral model, but has nothing to do with the fit process. Instead, from the residual map, we can see that the fit result is good since the differences in number of photon counts are very low — about 5% of the photon counts of the count map.

	Now		Previous	
	Value	Error	Value	Error
Index1 (γ_1)	1.89492	0.04044	2.0	0.1
Cutoff (E_c , MeV)	3766.69	397.38	4600	1200
Photon Flux ($\text{ph cm}^{-2}\text{s}^{-1}$) (10^{-8})	7.28913	0.27988	7.7	0.7

Table 2.4: *Fit parameters of the spectral model of PSR J0218+4232. The names of parameters are consistent with the equation 2.4. The old results are from the paper [1].*

< **change** > should rename "Previous" and "Now".

should draw a diagonal line in the upper left cell, but don't know how yet.)< **/change** >

The table 2.4 lists the results of fitting parameters. We see from the Fig. that the new fit results are consistent with the old results. However, the precision improves a lot which is ascribed to the Fermi LAT Third Source Catalogue and PASS 8 data. The Fig. 2.5 plot the spectrum according to the function 2.4. One thing should be noticed is that we need to multiply E^2 to the function 2.4 to get the flux. The Fig. 2.5 shows that the global fit is consistent with flux points fitted by each energy bin separately. The TS value for the fit is 7110, which gives us a significance level $\sigma \approx \sqrt{TS} = 84$. This strongly implies the presence of our target source. We can also use a TS map to test the presence of the source as the Figs 2.6 and 2.7 shown.

There are 2 sets of Ts maps with different scales. The first group is $3^\circ \times 3^\circ$

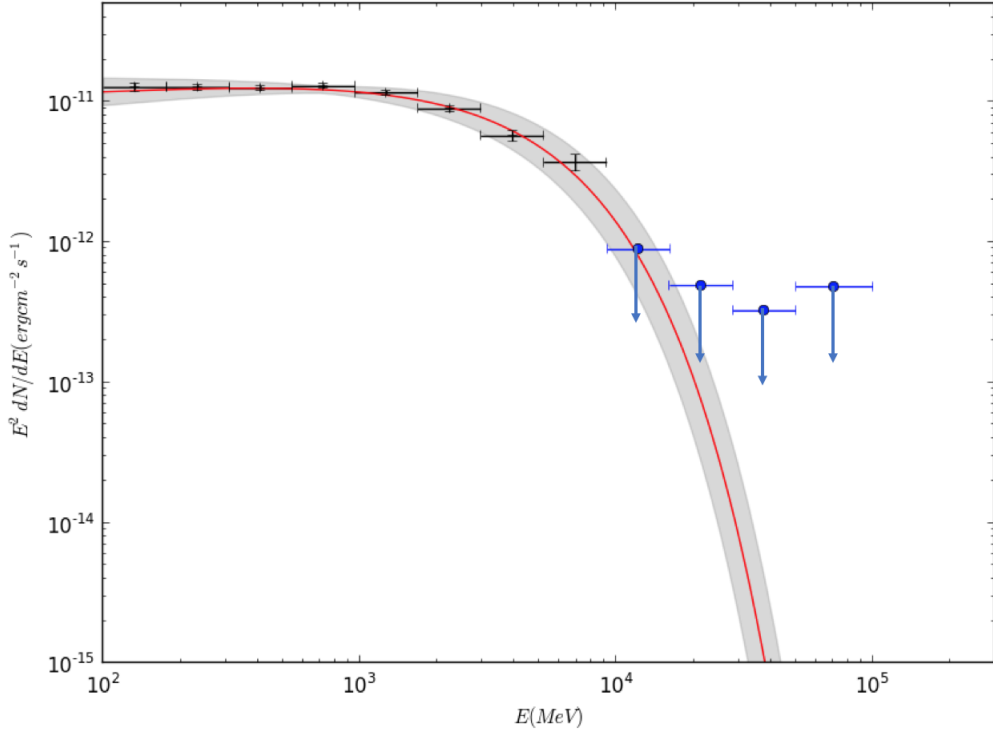


Figure 2.5: The log-log plot of flux to energy of PSR J0218+4232. The grey shade represents fitting errors, black points with error bars are flux points, the blue dots are upper values and the red line is the PLEXPcutoff model multiplied by E^2 . Flux points are fitted separately by dividing the total energy bin (100 MeV \sim 100 GeV) into multiple energy bins. The horizontal error bars represents the width of each bin.
(The Fig. should use legends, but for now I have problem setting those styles, may be my matplotlib version is too old.)

< **change** >legends, arrows< **/change** >

while the second group is $2^\circ \times 2^\circ$.

2.3.3 PSR B1821-24

The ROI region is a circle whose radius is 20° and all sources outside of 8° are fixed. There are 6 free sources in the region of 8° . The Fig. 2.8 is a combination of count maps of observation data and the model.

Count Maps And Count Cubes

The left and right part of the Fig. 2.10 is the count map of the PSR B1821-24 generate from observation data and spectral model respectively. Like the situations of PSR J0218+4232, the count map from the model is clearly cleaner than from the observation data and the two figures are very similar, which

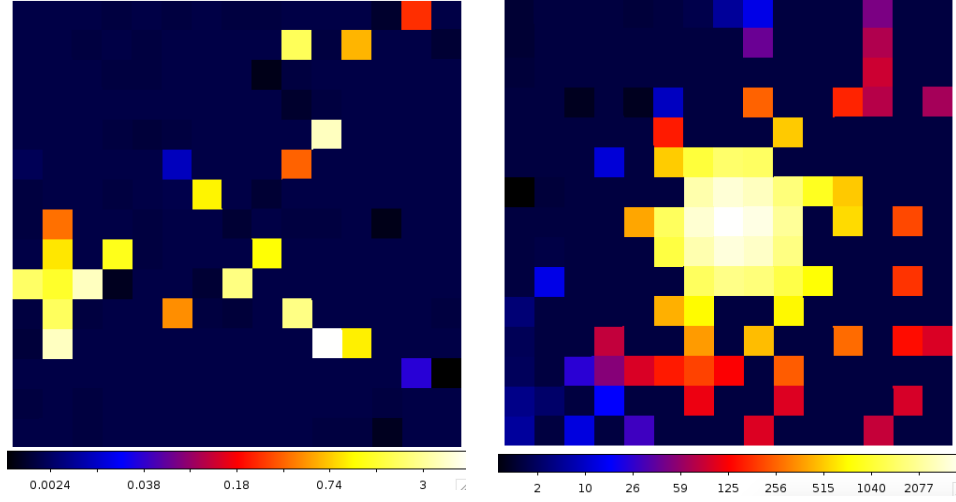


Figure 2.6: *TS maps of PSR J0218+4232. The Figs' dimensions are $3^\circ \times 3^\circ$ ($15\text{pixels} \times 15\text{pixels}$ with $0.25^\circ \times 0.25^\circ$ for each pixel). The left figure and right figure are generated by the XML models with and without our target source PSR J0218+4232 respectively. The left figure shows that the possibility of adding an imputative point source is very low only with a maximum TS value of less than 5. However, the right figure strongly implies that there should be an additional source after we have removed our target source from the model, which means it's very likely that PSR J0218+4232 is contained in our observation data.*

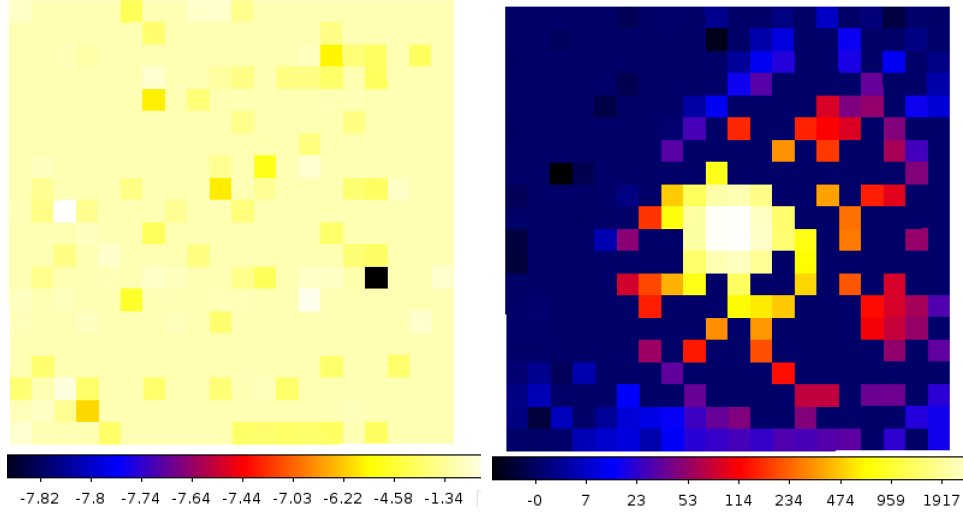


Figure 2.7: *TS maps for PSR J0218+4232. The Figs' dimensions are $4^\circ \times 4^\circ$ ($20\text{pixels} \times 20\text{pixels}$ with $0.25^\circ \times 0.25^\circ$ for each pixel). The Figs meanings are completely the same with the Fig. 2.6*

implies that our model is close to the observation.

The Figs 2.9 are count maps of PSR B1821-24 in different energy bands. The target pulsar is too faint in very high energy band and interfered too much by the ambient environment in low energy band (around 100MeV). Because our target source is near the M28 globular cluster and very faint, it is reasonable

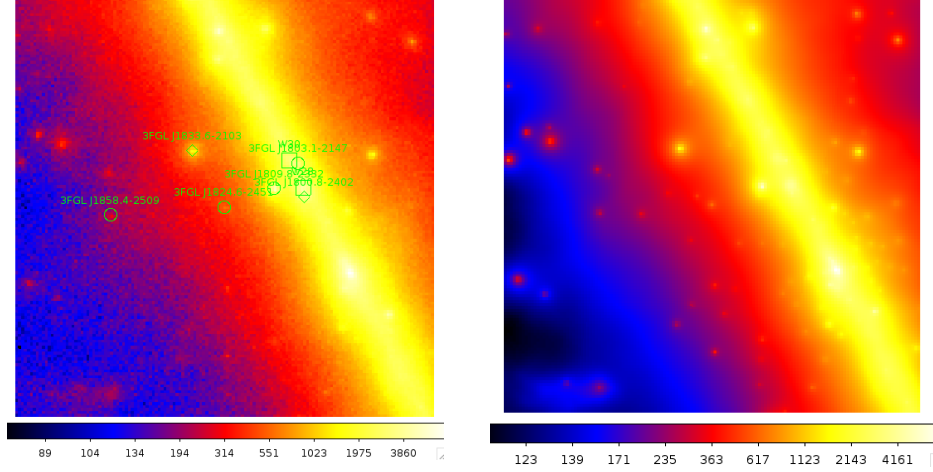


Figure 2.8: The count map of PSR J1824.6 (left) and the count map generated by the model. In the left figure, the green circles are free sources. The sizes of the both figures are $141 \text{ pixels} \times 141 \text{ pixels}$, and each pixel is $0.2^\circ \times 0.2^\circ$.

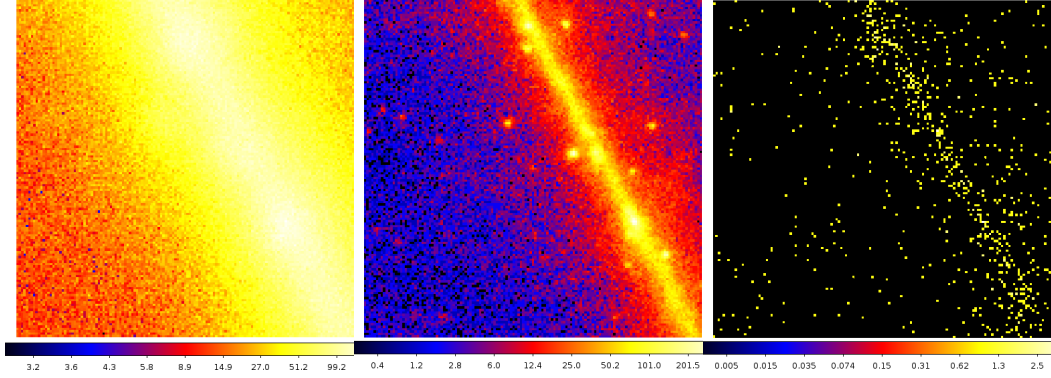


Figure 2.9: Three figures of PSR B1821-24's count cube. The energy range of the Fig. in the left: $100 \sim 123 \text{ MeV}$, middle: $1.873 \sim 2.310 \text{ GeV}$, right: $81.11 \sim 100 \text{ GeV}$.

that the fitting result is worse than PSR J0218+4232.

Binned Likelihood Analysis

The differences of the count map between the observation data and the model are described as the Fig. 2.10 which are in linear scale. In the right part of the Fig., there are some black dots with value of about -800 . Though their values are relatively high, the number of high-value dots are very small so the fit is acceptable in general.

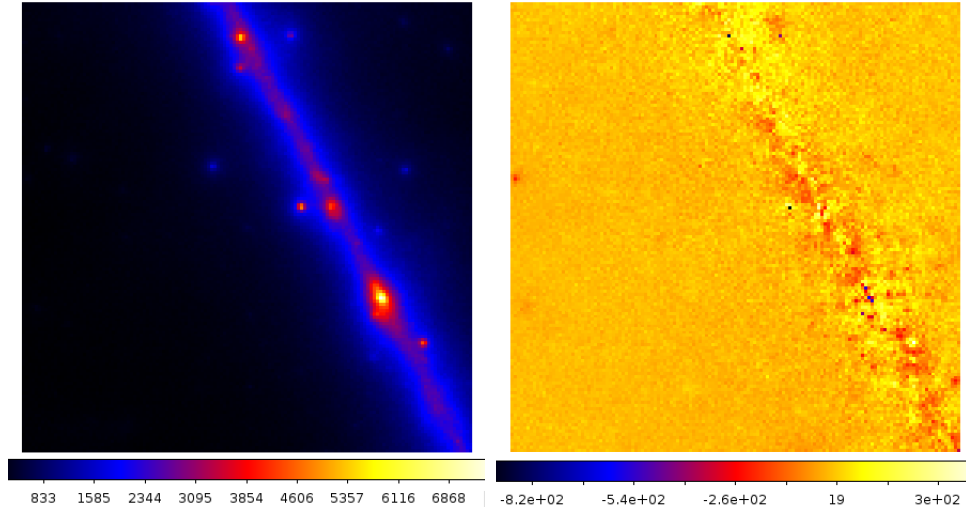


Figure 2.10: The count map and residual map of PSR B1821-24 in linear scale. The left figure is the count map and the right figure is the residual map showing the difference between the observation and the model.

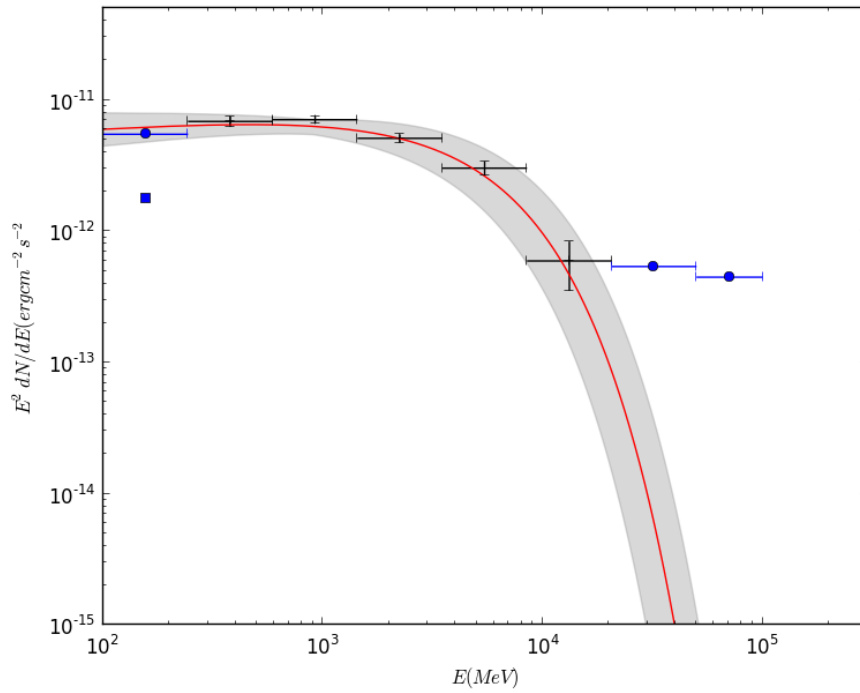


Figure 2.11: The log-log plot of flux to energy. < change > should use legends, add arrows for upper values, make the label fonts larger. < /change >

The table 2.5 shows the global fit results of PSR B1821-24. < mayChange > There is no previous fit results for the pulsar, so we cannot compare our result with the old one. < /mayChange > The TS value of the model is 941 which gives us a significance level of about $\sqrt{941} \sim 31$. This strongly shows the existence

of the target source in the observation data.

The Fig. 2.11 shows that the global fit is consistent with the flux points generated by fitting sub-energy bins. However, we should notice the first flux point which is denoted as a blue square in the Fig. 2.11. This flux point is significantly smaller than the global fit (the red line in the Fig.). In addition, the upper value for the first energy bin is still slightly smaller than the global fit. Though it is strange that the upper value is smaller than the normal value at first glance, it is reasonable since the flux points are fitted separately and are independent to the global fit. In fact, we use a single power-law model to fit each sub-energy bin while PLEXPcutoff model to do the global fit. As we have explained previously, the lower energy part of the observation (around 100 MeV) is not as reliable as other energy bands. As a result, the separate fit for the first energy bin is not as reliable as the global fit and it is reasonable that the two fitting results are not consistent. When this happens, we have more confidence on the global fit than the separate fit.

	Now		Previous	
	Value	Error	Value	Error
Index1 (γ_1)	1.906	0.068	<i>Nan</i>	<i>Nan</i>
Cutoff (E_c , MeV)	4501.92	710.41	<i>Nan</i>	<i>Nan</i>
Photon Flux ($\text{ph cm}^{-2}\text{s}^{-1}$) (10^{-8})	3.85	0.31	<i>Nan</i>	<i>Nan</i>

Table 2.5: *Fit parameters of the spectral model of PSR B1821-24. The names of parameters are also consistent with the equation 2.4. <question>The old results are not available yet</question>*

< change >should rename "Previous" and "Now".

should draw a diagonal line in the upper left cell, but don't know how yet.)< /change >

2.3.4 PSR B1937+21

In order to make the data analysis be more consistent, we choose the same parameters to process the observation data. Like the other two MSPs, the radius of ROI is 20° degrees, and all parameters of sources 8° degrees outside from

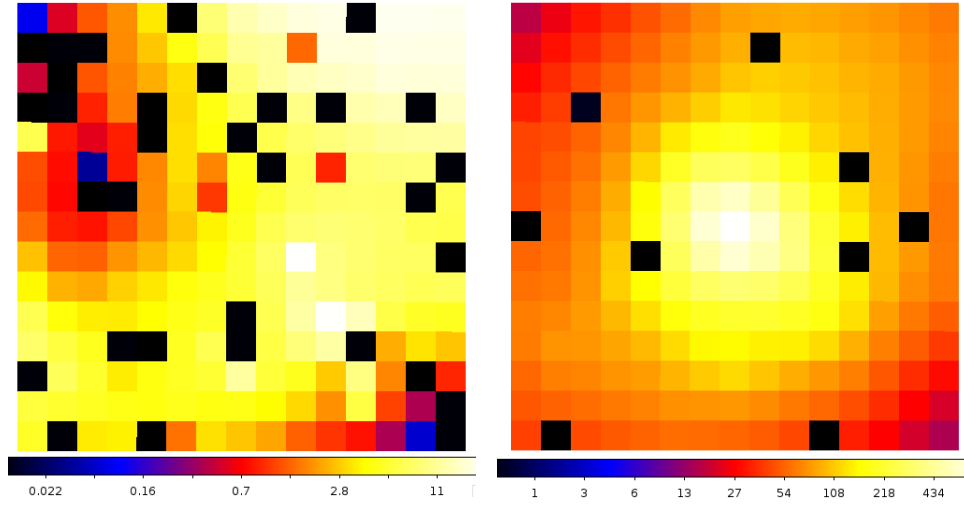


Figure 2.12: *TS maps of PSR B1821-24. The Fig.s' dimensions are $3^\circ \times 3^\circ$ ($15\text{pixels} \times 15\text{pixels}$ with $0.25^\circ \times 0.25^\circ$ for each pixel). The left figure and right figure are generated by the XML models with and without our target source PSR J1821.6-2452 respectively. The left figure shows that the possibility of adding an imputative point source is very low only with a maximum TS value of less than 11 and the TS values of the right figure are generally much larger.*

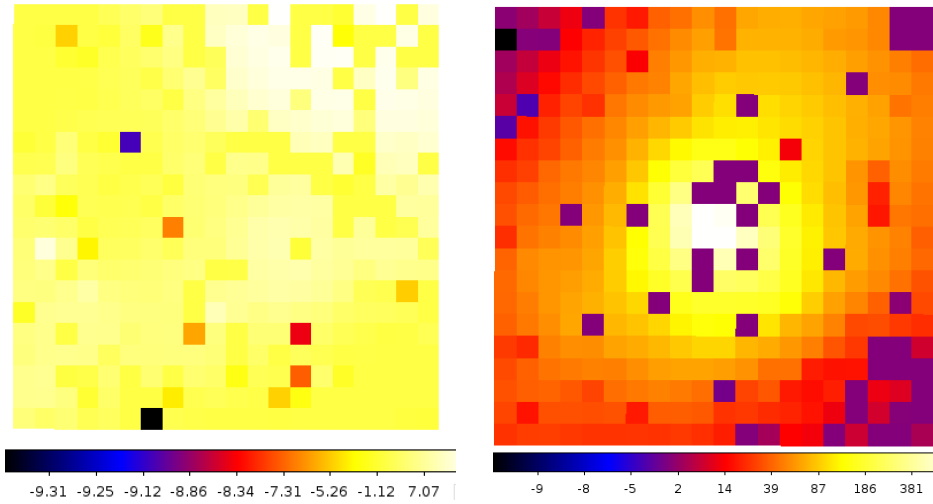


Figure 2.13: *TS maps of PSR B1821-24. The Fig.s' dimensions are $4^\circ \times 4^\circ$ ($20\text{pixels} \times 20\text{pixels}$ with $0.25^\circ \times 0.25^\circ$ for each pixel). The meaning of the figure is the same as the Fig. 2.13*

the center are fixed with default values. The Fig. 2.14 shows the comparison of count maps between observation data and our spectral model.

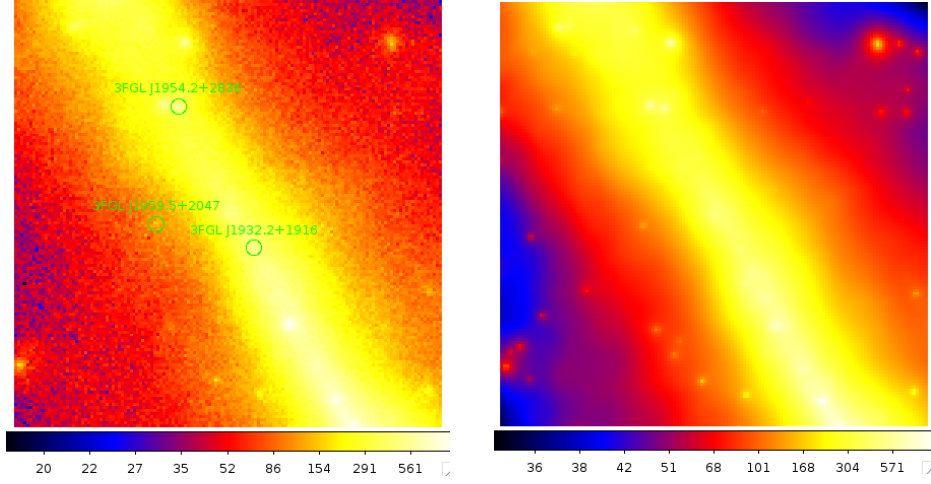


Figure 2.14: The count map of PSR B1937+21 created from observation data (left) and from the spectral model (right). The dimensions of both figures are $141\text{pixels} \times 141\text{pixels}$ and each pixel is $0.2^\circ \times 0.2^\circ$ large.

Count Maps and Count Cubes

There are 4 point sources with free parameters in the model which are represented by the green circles in the Fig. 2.14. However, the left part of the Fig. 2.14 only contains three circles. This is the difference between the PSR B1937+21 and the other two MSPs described above. With some reasons, the PSR B1937+21 is not shown in Fermi LAT Third Source Catalogue. Therefore, in order to analysis the spectrum of this pulsar, we have to add the source by hand. The green circles are only created by Fermi tools by default, hence our source is not represented by a green circle. In addition, the count map is so messy that we completely cannot distinguish the source PSR B1937+21 from the count map. Since our target pulsar PSR B1937+21 is not in the Fermi LAT Third Source Catalogue and we have to generate the model by hand, we need to set the model with its parameters properly. Like the other 2 MSPs, we choose the specified PLSuperExpCutoff model and set the initial value of photon index to be -2.5 .

The Fig. 2.15 shows count maps in difference energy bands. As the Fig. shown, the lower energy band is too messy while there is nearly nothing valuable in the high energy band. Therefore, when we divide the total energy bin into many sub-bins to do analysis separately, we focus on the middle parts and have more bins in that range of energy.

<add>Continue from here...

PSR B1937+21 is a little bit different. I did a phase resolved analysis, in order to show if it is necessary, I plan to do a new phase averaged analysis for

comparison. The best phase averaged results are not finished completely yet, but soon.</add>

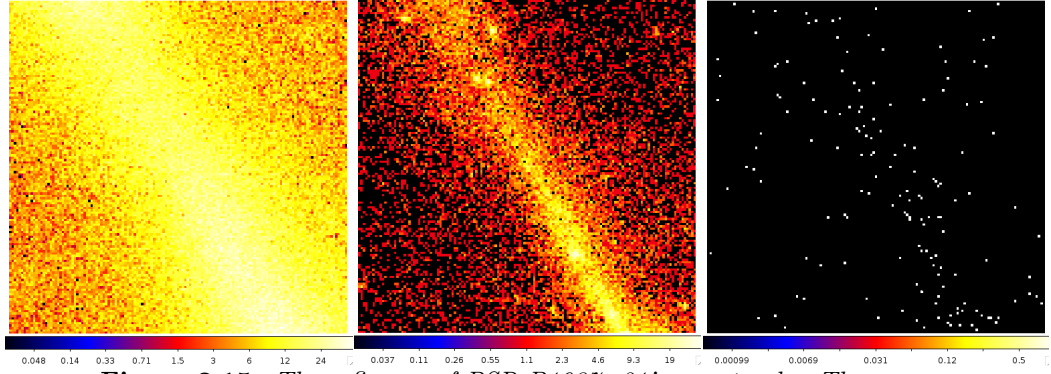


Figure 2.15: Three figures of PSR B1937+21's count cube. The energy range of the Fig. in the left: 100~123MeV, middle: 1.873~2.310GeV, right: 35.11~43.29GeV.

Binned Likelihood Analysis

The Fig. 2.16 shows the residual map together with the original count map in linear scale.

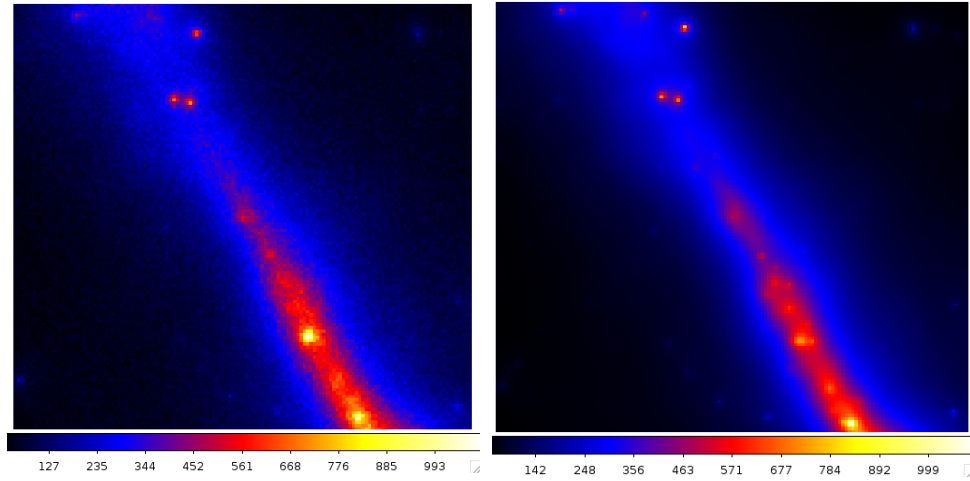


Figure 2.16: The count map of PSR B1937+21 created from observation data (left) and from the spectral model (right). The dimensions of both figures are 141pixels \times 141pixels and each pixel's size is $0.2^\circ \times 0.2^\circ$.

Chapter 3

Theory And Simulation

3.1 Two-layer Model

After we have reviewed gamma-ray fundamental emission mechanism, we can proceed to the Two-layer model on which this thesis is mainly based. Two-layer model is a variation of outer-gap model since they both claim that the gamma-ray emission zone is close to the light-cylinder. However, in two-layer model, the outer layer consists of two regions — a primary acceleration region and a screening region.

In the primary region, charged particles moved out of pulsars along the open field lines, so the charge density is usually very low. However, by pair-production processes, a lot of e^- and e^+ are produced. But in the primary region where lots of pairs are created, the charge density doesn't change very much because the pairs have not been separated yet. With the help of strong electric field, the particles of different signs move to opposite directions. As a result, the two-layer model states that just above the primary region, a screening region will be created and the charge density is very large. This is basically the reason why there are two regions in pulsars' outer magnetosphere.

Then the next issue is that how we describe the distribution of charge density in these two regions. For simplicity, we just use a step function to represent the charge density distribution and step function can clearly shows the gap between the two regions. We use a magnetic dipole model to approximate the magnetic distribution in the magnetosphere. Since in magnetic dipole model, magnetic field at one position is only dependent on the position's distance from the source and altitude, we can also ignore the azimuthal distribution of charge density in our model and use the two parameters the $r(distance)$ and $\theta(altitude)$ to calculate the magnetic field at some position.

In the two-layer model, we can use three parameters to express the structure of a pulsar's outer magnetosphere - charge density of the primary region, the

total length of the primary region and the screening region and the last one is the ratio of the thickness of the primary region and the screening region. The Fig. 3.1 shows the basic structure of two-layer model.

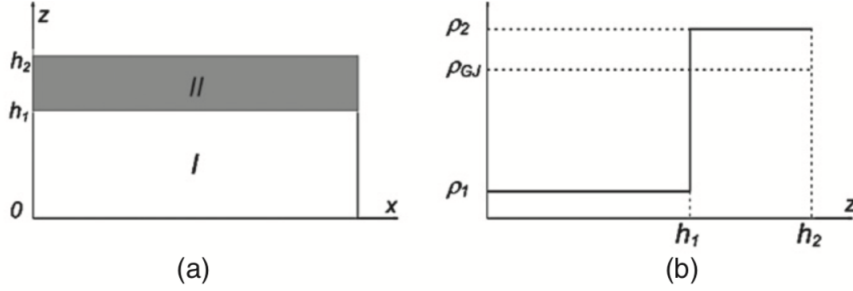


Figure 3.1: (a): The geometry of two-layer model. h_1 and h_2 is the height of the primary region and the screening region respectively. (b): the charge densities of primary region and screening region. In the primary region, the charge density is much smaller than Goldreich-Julian charge density while is larger in the screening region. < mayChange > this figure is from the previous paper, I may need to regenerate the Fig..< /mayChange >

As the Fig. 3.1 showing, let the charge density of the primary region be $\rho_1 = (1 - g_1)\rho_{GJ}$ and the total gap size is h_2 , where ρ_{GJ} is Goldreich-Julian charge density. For convenience, we also denote the gap size of the primary region as h_1 .

We denote the electrical potential to be ϕ_0 which satisfies

$$\nabla^2 \phi_0 = -4\pi \rho_{GJ} \quad (3.1)$$

and the total electrical potential is $\phi = \phi_0 + \phi'$, where ϕ' is a representation of the deviation of the co-rotating electrical potential. Let total charge density is ρ and subtract the equation 3.1 we have

$$\nabla^2 \phi' = -4\pi (\rho - \rho_{GJ}) \quad (3.2)$$

Because the model has ignored the distribution in the azimuthal direction, we can use two parameters x, z to represent a position, where x is the direction along the magnetic field line and z is the perpendicular to the magnetic field line. In order to solve the equation 3.2, the model also makes 2 approximations. The first is that the directive of electrical potential ϕ is ignored. The second is that the Goldreich-Julian charge density is uniformly distributed along the magnetic line direction (x direction). These 2 approximations are based on the a reasonable assumption that the change rate for both electrical potential (ϕ') and Goldreich-Julian charge density (ρ_{GJ}) along the x direction is much smaller compared with z direction. As a result, the equation 3.2 can be written as:

$$\frac{\partial^2}{\partial z^2} \phi' = -4\pi (\rho - \rho_{GJ}) \quad (3.3)$$

In order to solve the equation 3.3, we have to have proper boundary conditions. First of all, we have to decide the boundary positions, which is determined by 4 parameters and they are $x_{lo}, x_{hi}, z_{lo}, z_{hi}$. It is reasonable to set x_{lo} and x_{hi} be the pulsar's surface and the light cylinder respectively and z_{lo} (lower boundary) be the last open field line. And let the electrical potential be 0 along the last open field line (this is because we have ignored the variation of electric field in x direction).

$$\phi(x, z_{lo}) = 0 \quad (3.4)$$

The position of z_{hi} is a little bit tricky. In order to make the electrical potential be continuous at $z = z_{hi} = h_2$, the model sets the $\phi'(z = h_2) = 0$ since the non-corotating electrical potential outside the upper bound is 0 and the co-rotating potential is continuous near the boundary. Additionally, because $\phi'(z = h_2-) = 0$ and $\phi'(z = h_2+) = 0$, we know that the first order derivative $\partial\phi'/\partial z|_{z=h_2}$ is 0, which means $E_\perp|_{z=h_2} = 0$. In order to solve the equation 3.3, we denote charge densities of the two regions for convenience as the following function 3.5 shown.

$$\rho(z) = \begin{cases} \rho_1, & \text{if } (0 \leq z < h_1) \\ \rho_2, & \text{if } (h_1 \leq z \leq h_2) \end{cases} \quad (3.5)$$

With the definition 3.5 and the three boundary conditions we can directly solve the equation 3.3 and the result is:

$$\phi'(z, x) = -2\pi \begin{cases} (\rho_1 - \rho_{GJ}(x)) z^2 + C_1 z, & (0 \leq z < h_1) \\ (\rho_2 - \rho_{GJ}(x)) (z^2 - h_2^2) + D_1 (z - h_2), & (h_1 \leq z \leq h_2) \end{cases} \quad (3.6)$$

where

$$C_1 = \frac{(\rho_1 - \rho_{GJ}(x)) h_1 (h_1 - 2h_2) - (\rho_2 - \rho_{GJ}(x)) (h_1 - h_2)^2}{h_2}$$

$$D_2 = \frac{(\rho_1 - \rho_2) h_1^2 - (\rho_2 - \rho_{GJ}(x)) h_2^2}{h_2}$$

From equation 3.6 and apply $\rho_{GJ}(x) = -(\Omega B x) / (2\pi c s)$ we can directly derive the electrical field parallel to magnetic field lines as a function of z as the equation 3.7 shown.

$$E'_\parallel(z) = \frac{\Omega B}{cs} \begin{cases} -g_1 z^2 + C'_1 z, & (0 \leq z < h_1) \\ g_2 (z^2 - h_2^2) + D'_1 (z - h_2) & (h_1 \leq z \leq h_2) \end{cases} \quad (3.7)$$

where

$$C'_1 = \frac{g_1 h_1 (h_1 - 2h_2) + g_2 (h_1 - h_2)^2}{h_2}$$

$$D'_2 = -\frac{(g_1 + g_2) h_2^2 + g_2 h_2^2}{h_2}$$

Since charged particles are accelerated in the primary region to relativistic speed and then emit energy by curvature radiation, we have equation 3.8.

$$eE'_{\parallel}c = l_{cur} \quad (3.8)$$

where E'_{\parallel} is the electric field strength along the magnetic field line described in equation 3.7. We can estimate Lorentz factors of the charged particles according to the function 3.9.

$$l_{cur} = \frac{2e^2c\gamma_e^4}{3s^2} \quad (3.9)$$

where s is the radius of curvature. Combining the equation 3.8 and 3.9 we get Lorentz factor:

$$\gamma_e = \left(\frac{3s^2}{2e} E'_{\parallel} \right)^{1/4} \quad (3.10)$$

With Lorentz factor of charged particles known, we can derive curvature radiation spectrum for single charged particle and then can get the total spectrum by integrating over all charged particles. This is the simplified basic idea of the Two-layer model.

Constraints of The Two-layer Model Used In The Thesis

The simplified two-layer model is consistent with observation data to some extent. (The relevant data can be found in the paper [9]) The model uses 4 parameters to get a fair good prediction of gamma-ray spectra for many pulsars. And all these 4 parameters have a very obvious physical meaning. However, we can clearly find the "defects" of the model — it is somewhat oversimplified. Though there are other more sophisticated version of two-layer model, we use the simpler one, which may cause some inconsistency between our simulation and observation.

Therefore, we can briefly analyze which part is oversimplified and can be improved. First of all, we directly use a step function to describe the charged particle distribution. Though the charge density of the screening region is much larger than the primary region, using a step function is non-physical and may exaggerate the change rate of charge density. At the same time, the dramatic change of charge density also brings introduces some instability for numerical simulation.

Secondly, the model sets the total of screening region and primary region to be rectangular shape. Though the shape is not clear, it should not be a rectangular in theory and may be very different. In numerical simulation, changes in shape of the regions will directly lead to a different integration region, which may change the simulated spectra completely.

Thirdly, there are some inconsistency in the model itself according to the its assumption. According to the equations 3.9 and 3.10 since E'_{\parallel} can be 0, we

know that γ_e can also be 0, which is absolutely impossible. Although this may not have a big influence on the spectra, it is the problem that we should solve.

All in all, the model is simple and the gamma-ray spectra computed based on the model is consistent with observation data. There are many much more sophisticated two-layer model which are generalizations of model used in the thesis. Those models may have addressed the problems described above, but the model used in the thesis do have some defects.

3.2 Numerical Calculation of Spectra Based on Two-layer Model

After we have understood theory part of the two-layer model, we can then do numerical calculations of spectra based on the theory. Since the theory is the same for all the three MSPs, the calculation algorithms are the same.

There are 3 independent parameters to fit altogether in the calculation. The first parameter is fractional gap size $f = h_2/R_{lc}$, where h_2 is the total gap size including both the primary acceleration region and the screening region and R_{lc} is the length of light cylinder. The second parameter is g_1 so that the charge density in the primary accelerating region is $(1 - g_1)\rho_{GJ}$, where ρ_{GJ} is the Goldreich-Julian charge density. The third parameter is the ratio between the sizes of the two gaps (h_1/h_2). Note that we only set the charge density in the primary acceleration region as an independent parameter, since the charge density in the two gaps are related to each other. The Figs 3.2 are the spectra of the three MSPs generate from the two-layer model and the result of the fitting parameters are listed in the table 3.1. Other than the low energy and high energy gamma-ray bands, the model is consistent with the observation data in terms of gamma-ray part.

Generally speaking, the modeled spectra for the three MSPs are acceptable. Just as we have discussed in the data analysis part that global fits are not very consistent with separate fits in low energy gamma-ray band (about $100MeV \sim 1000MeV$) and high energy band (above $10GeV$), the modeled spectra also have the same problem. This can have 2 explanations. Firstly, the Fermi telescope is not sensitive in about $100MeV$. As a result, the observation data may not be very reliable at about this energy band. Secondly, the real emission mechanism in the energy band is different from the model predicts. Thus, we can observe inconsistency between the calculations and observations.

After obtaining the spectra fit results in gamma-ray band, we can generate

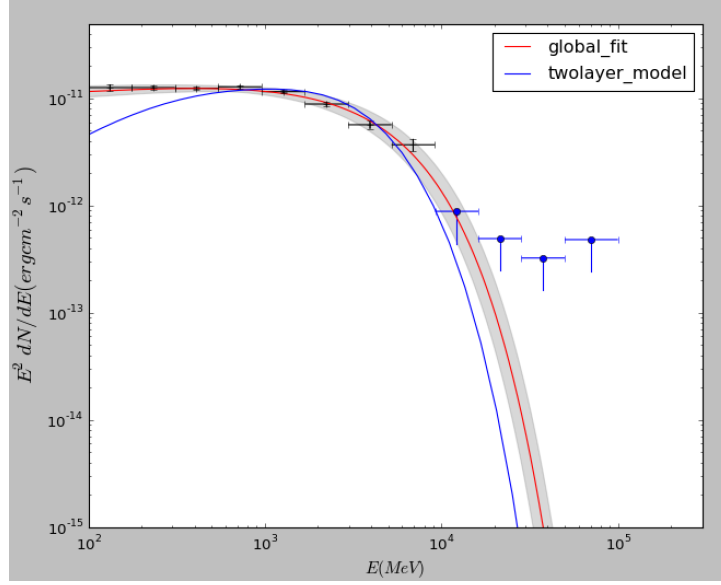


Figure 3.2: The modeled spectrum of PSR J0218+4232. < change >python arrow doesn't work properly< /change >

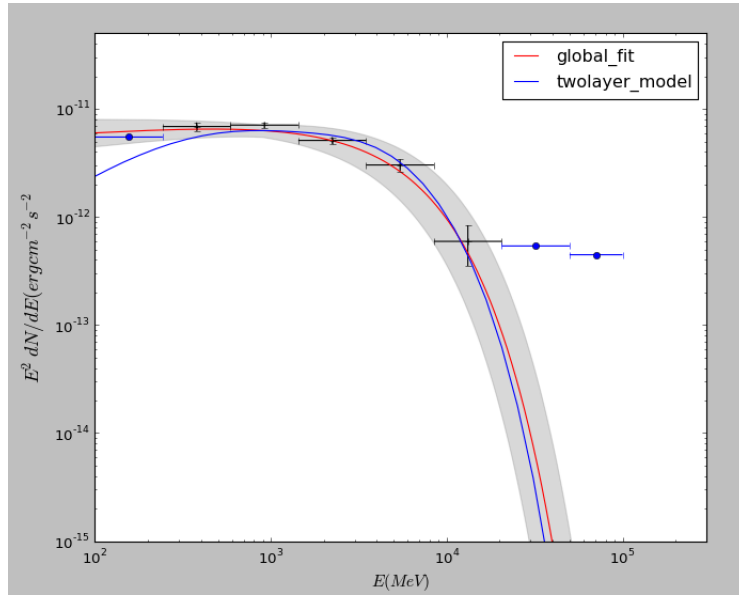


Figure 3.3: The modeled spectrum of PSR B1821-24. < mayChange >I wanted to combine the three figures together, if I do so, each figure is too small.< /mayChange >

broad band spectra as the Figs 3.5 shown. The hard X-ray data are from the paper [2]. By tweaking the independent parameters of the two-layer model, we can make the modeled spectra very close to the observation data in hard X-ray band. Since we lack observation data in the energy band from about 100keV to 100MeV, we cannot tell if the two-layer model describes the right physical scenario in this energy range. However, the prediction made by the simplified two-layer model is relatively precise. In addition, the model is very intuitive, which is also a very important consideration for building a model. Just as the

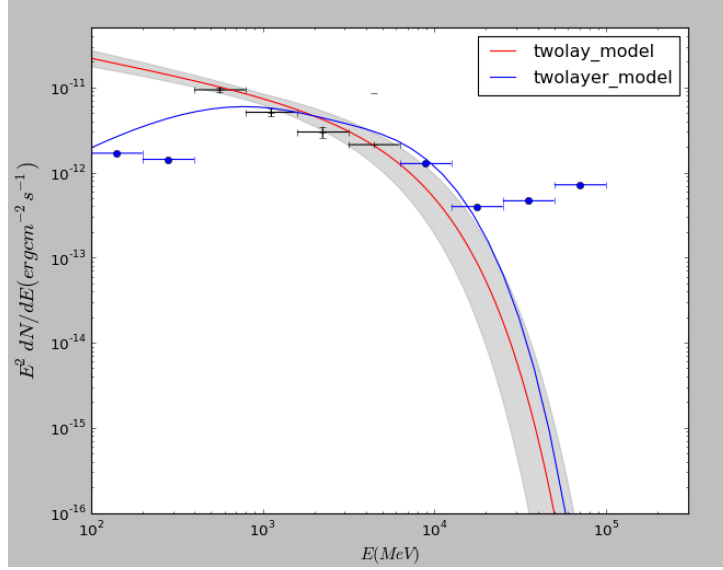


Figure 3.4: *The modeled spectrum of PSR B1937+21.*

	f	g	h_1/h_2
PSR J0218+4232	0.330	0.92	0.915
PSR J0218+4232	0.247	0.955	0.920
PSR J0218+4232	0.320	0.975	0.925

Table 3.1: *The results of fitting parameters for the three MSPs. The physical meaning of each parameter is consistent with the two-layer model describe above. <change>the table is ugly, but not sure how to make it more beautiful...</change>*

famous words "With four parameters I can fit an elephant, and with five I can make him wiggle his trunk" said by John von Neumann, in principal, we can fit any data by adding independent parameters. Therefore, in order to test if a theory model is good or not, not only we need to consider how precisely the model can predict, but also the physical meaning behind the model. In this sense, the two-layer model is a good start of explaining emission mechanism of pulsars.

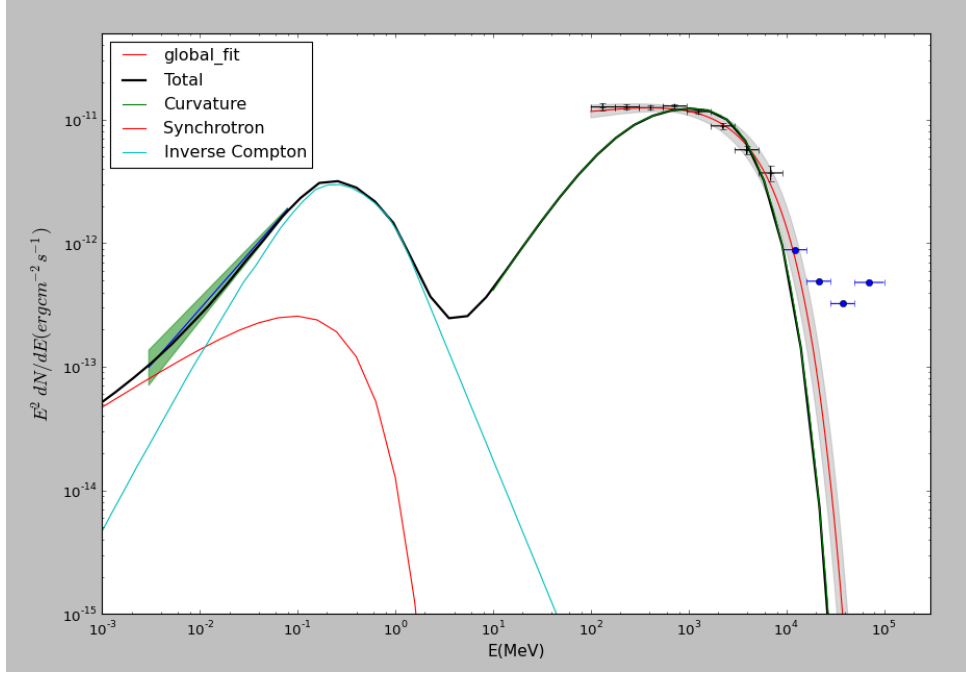


Figure 3.5: The broad band and modeled spectrum of PSR J0218+4232. The grey shade is the error of the global fit. And the green shade in the left part of the figure represents the error of hard X-ray. The 'Total' legend represents the total flux combining the Synchrotron radiation, inverse Compton radiation and curvature radiation altogether.

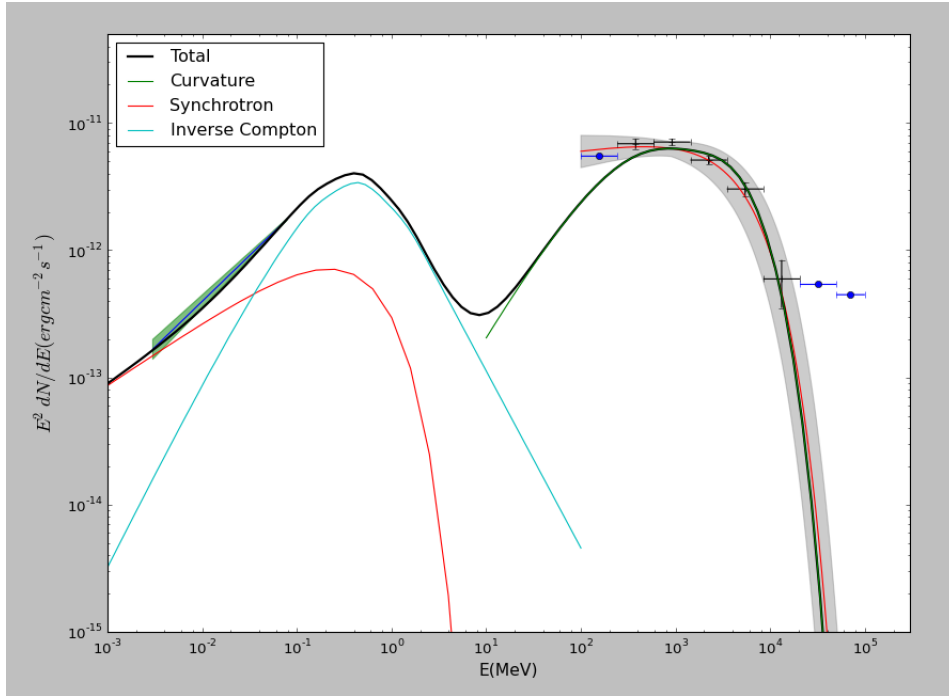


Figure 3.6: The broad band and modeled spectrum of PSR B1821-24. The meaning of grey shade and the green shade are the same as the Fig. 3.5

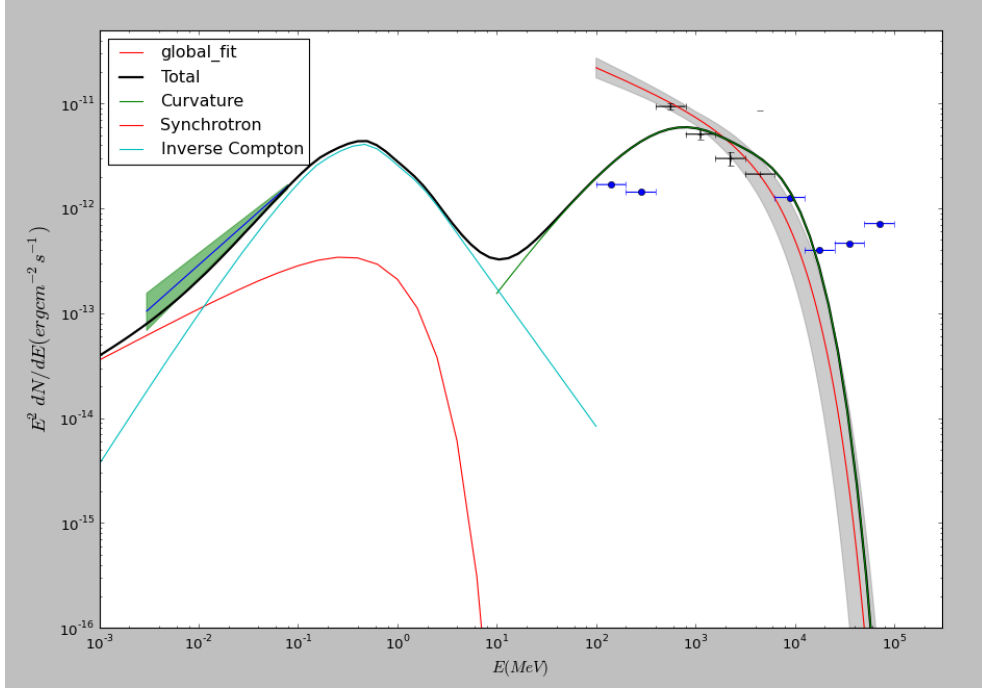


Figure 3.7: The broad band and modeled spectrum of PSR B1937+21. The meaning of grey shade and the green shade are the same as the Fig. 3.5

3.3 Pitfalls and Considerations of Doing Numerical Calculation

3.3.1 Correctness of Computation

To make sure the numerical computation be right is the most important. The first consideration is underflow and overflow of floating digits. One possible condition is calculating speed of relativistic charged particles with Lorentz factor γ . By doing some simple test, we find that for $\gamma < 1.5 \times 10^7$, the results are precise enough. However, there is significant rounding error when $\gamma > 5 \times 10^7$, which means that our results will be wrong for highly energetic particles if we directly use the formula $\beta = \sqrt{1 - 1/\gamma^2}$. Likely, in the two-layer model, nearly all particles have $\gamma < 1 \times 10^7$. Furthermore, there are nearly no situations where double precision floating digits cannot handle calculation results of the two-layer model. Thus, as long as we use 64-bit floating digits instead of 32-bit floating digits, we are free from overflowing and underflow troubles.

There are some cases when a whole function can be calculated while some parts of them are not. Take the function $f(x) = x \times 1/x$ for example. When x is too large, it can not be expressed by a computer and multiplication is not associative when doing floating point operation. We encounter some situations like this. The formula of curvature radiation spectrum contains modified Bessel

function of order $5/3$. In order to speed up the program, we use a polynomial to express the Bessel function, as the function 3.11 shown.

$$K_{5/3}(x) \simeq a \left(\frac{1}{x} + b \right)^{-cx-1/3} \sqrt{\frac{\pi}{2}} e^{-x-d} \sqrt{x+d} \left[1 + \frac{55}{72(x+d)} - \frac{10151}{10368} (x+d)^2 \right] \quad (3.11)$$

where a, b, c, d are just positive constants and $c = 0.96 < 1$. As a result, the part $(1/x + b)^{-cx-1/3}$ in the function 3.11 is infinity when x is large though the total function is approximated to 0. Thus, we have to explicitly assign the result to be 0 instead of calculating it. Actually, this error is not easy to find since in most cases the result is not infinity.

3.3.2 Speed of Computation

We actually have not done any accurate benchmarks for the following discussions and they are dependent of the average time of running the simulation. The most obvious solution of to use multicores to do computation. However, most library functions do not support run concurrently and only run on a single core. For example, we need to do many integrations and the speed of integration is critical. We write some simple functions to utilize 4 CPU cores at the same time when doing integration. This gives us a huge performance improvement.

Furthermore, There are some facts about the basic operations. For instance, add is faster than multiplication which is faster than deviation. Multiplications and deviations are not associative between floating points. Though the performance differences between different operations for integers can usually be optimized away by modern compilers, the compilers can do nothing for floating points. Thus, we have to do it by ourselves. For example, we have $z^2 - h_2(x)^2$ in function 3.7. In this formula, we have 2 multiplications and 1 subtraction. After we re-write it to $(z - h_2)(z + h_2)$, we have 1 addition, 1 subtraction and 1 multiplication. Since addition and subtraction is not slower than multiplication, it has no performance harm for the rewriting. What we need to notice is that the multiplication may not be slower than addition and it is dependent on machines. However, division is definitely slower than the other 3 operations. Therefore, in our program, expressions like $1/3$ are rewritten to $1 * 0.3333$ and so on.

Chapter 4

Discussion and Future Work

<add>continue from here...</add>

References

- [1] A. A. Abdo, M. Ajello, A. Allafort, L. Baldini, J. Ballet, G. Barbiellini, M. G. Baring, D. Bastieri, A. Belfiore, R. Bellazzini, B. Bhattacharyya, E. Bissaldi, E. D. Bloom, E. Bonamente, E. Bottacini, T. J. Brandt, J. Bregeon, M. Brigida, P. Bruel, R. Buehler, M. Burgay, T. H. Burnett, G. Busetto, S. Buson, G. A. Caliandro, R. A. Cameron, F. Camilo, P. A. Caraveo, J. M. Casandjian, C. Cecchi, Ö. Çelik, E. Charles, S. Chaty, R. C. G. Chaves, A. Chekhtman, A. W. Chen, J. Chiang, G. Chiaro, S. Ciprini, R. Claus, I. Cognard, J. Cohen-Tanugi, L. R. Cominsky, J. Conrad, S. Cutini, F. D’Ammando, A. de Angelis, M. E. DeCesar, A. De Luca, P. R. den Hartog, F. de Palma, C. D. Dermer, G. Desvignes, S. W. Digel, L. Di Venere, P. S. Drell, A. Drlica-Wagner, R. Dubois, D. Dumora, C. M. Espinoza, L. Falletti, C. Favuzzi, E. C. Ferrara, W. B. Focke, A. Franckowiak, P. C. C. Freire, S. Funk, P. Fusco, F. Gargano, D. Gasparrini, S. Germani, N. Giglietto, P. Giommi, F. Giordano, M. Giroletti, T. Glanzman, G. Godfrey, E. V. Gotthelf, I. A. Grenier, M.-H. Grondin, J. E. Grove, L. Guillemot, S. Guiriec, D. Hadasch, Y. Hanabata, A. K. Harding, M. Hayashida, E. Hays, J. Hessels, J. Hewitt, A. B. Hill, D. Horan, X. Hou, R. E. Hughes, M. S. Jackson, G. H. Janssen, T. Jogler, G. Jóhannesson, R. P. Johnson, A. S. Johnson, T. J. Johnson, W. N. Johnson, S. Johnston, T. Kamae, J. Kataoka, M. Keith, M. Kerr, J. Knödseder, M. Kramer, M. Kuss, J. Lande, S. Larsson, L. Latronico, M. Lemoine-Goumard, F. Longo, F. Loparco, M. N. Lovellette, P. Lubrano, A. G. Lyne, R. N. Manchester, M. Marelli, F. Massaro, M. Mayer, M. N. Mazzotta, J. E. McEnery, M. A. McLaughlin, J. Mehault, P. F. Michelson, R. P. Mignani, W. Mitthumsiri, T. Mizuno, A. A. Moiseev, M. E. Monzani, A. Morselli, I. V. Moskalenko, S. Murgia, T. Nakamori, R. Nemmen, E. Nuss, M. Ohno, T. Ohsugi, M. Orienti, E. Orlando, J. F. Ormes, D. Paneque, J. H. Panetta, D. Parent, J. S. Perkins, M. Pesce-Rollins, M. Pierbattista, F. Piron, G. Pivato, H. J. Pletsch, T. A. Porter, A. Possenti, S. Rainò, R. Rando, S. M. Ransom, P. S. Ray, M. Razzano, N. Rea, A. Reimer, O. Reimer, N. Renault, T. Reposeur, S. Ritz, R. W. Romani, M. Roth, R. Rousseau, J. Roy, J. Ruan, A. Sartori, P. M. Saz Parkinson, J. D. Scargle, A. Schulz, C. Sgrò, R. Shannon, E. J. Siskind, D. A. Smith, G. Spandre, P. Spinelli, B. W. Stappers, A. W. Strong, D. J.

- Suson, H. Takahashi, J. G. Thayer, J. B. Thayer, G. Theureau, D. J. Thompson, S. E. Thorsett, L. Tibaldo, O. Tibolla, M. Tinivella, D. F. Torres, G. Tosti, E. Troja, Y. Uchiyama, T. L. Usher, J. Vandenbroucke, V. Vasileiou, C. Venter, G. Vianello, V. Vitale, N. Wang, P. Weltevrede, B. L. Winer, M. T. Wolff, D. L. Wood, K. S. Wood, M. Wood, and Z. Yang. The second fermi large area telescope catalog of gamma-ray pulsars. *The Astrophysical Journal Supplement Series*, 208(2):17, 2013.
- [2] E. V. Gotthelf and S. Bogdanov. Nustar hard x-ray observations of the energetic millisecond pulsars psr b1821-24, psr b1937+21, and psr j0218+4232. *The Astrophysical Journal*, 845(2):159, 2017.
- [3] L. Guillemot, T. J. Johnson, C. Venter, M. Kerr, B. Pancrazi, M. Livingstone, G. H. Janssen, P. Jaroenjittichai, M. Kramer, I. Cognard, B. W. Stappers, A. K. Harding, F. Camilo, C. M. Espinoza, P. C. C. Freire, F. Gargano, J. E. Grove, S. Johnston, P. F. Michelson, A. Noutsos, D. Parent, S. M. Ransom, P. S. Ray, R. Shannon, D. A. Smith, G. Theureau, S. E. Thorsett, and N. Webb. Pulsed gamma rays from the original millisecond and black widow pulsars: A case for caustic radio emission? *The Astrophysical Journal*, 744(1):33, 2012.
- [4] O. Hamil, J. R. Stone, M. Urbanec, and G. Urbancová. Braking index of isolated pulsars. *Phys. Rev. D*, 91:063007, Mar 2015.
- [5] C.-Y. Ng, J. Takata, G. C. K. Leung, K. S. Cheng, and P. Philippopoulos. High-energy emission of the first millisecond pulsar. *The Astrophysical Journal*, 787(2):167, 2014.
- [6] Zakir F. Seidov. The roche problem: Some analytics. *The Astrophysical Journal*, 603(1):283, 2004.
- [7] P. A. Sturrock. A model of pulsars. *Astrophys. J.*, 164:529, 1971.
- [8] Hao Tong. Pulsar braking: magnetodipole vs. wind. *Science China Physics, Mechanics Astronomy*, 59(1):619501.
- [9] Y. Wang, J. Takata, and K. S. Cheng. Gamma-ray spectral properties of mature pulsars: A two-layer model. *The Astrophysical Journal*, 720(1):178, 2010.